Molecular Cell

Article

RNA anti-CRISPRs deplete Cas proteins to inhibit the CRISPR-Cas system

Graphical abstract

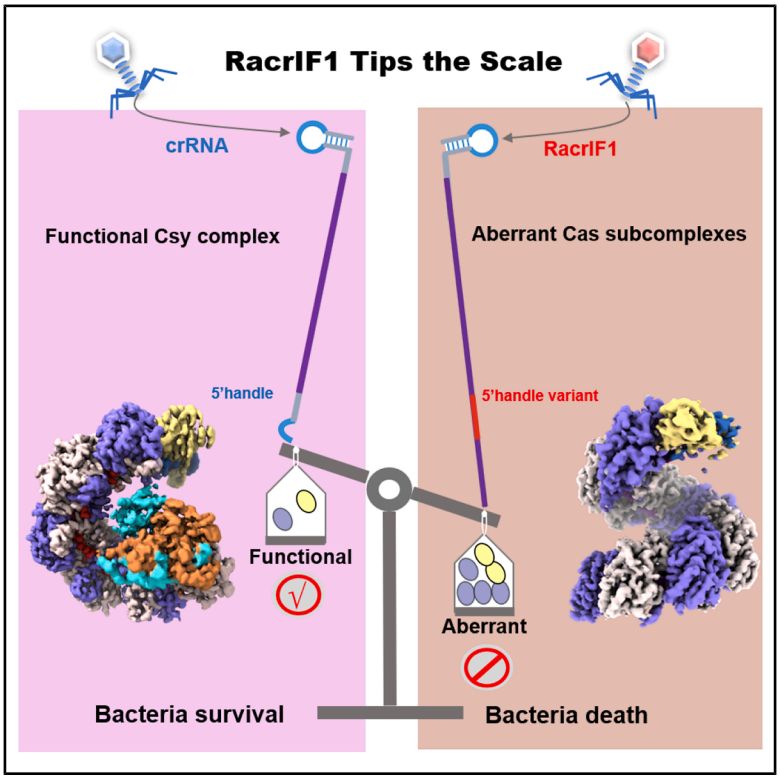

Highlights

- Cryo-EM structures identify Racr-induced aberrant Cas assemblies
- RacrIF1 5′-handle variant disrupts canonical Cas5f–Cas8f incorporation
- Racrs compete with crRNAs for shared Cas6f/Cas7f pools
- Cas7f forms right-handed superhelical filaments on non-specific RNA

Authors

Xiaopan Gao, Kaixiang Zhu, Weihe Zhang, ..., Xia Yu, Hongtao Zhu, Sheng Cui

Correspondence

gaoxiaopan@pumc.edu.cn (X.G.), yuxia@mail.ccmu.edu.cn (X.Y.), hongtao.zhu@iphy.ac.cn (H.Z.), cui.sheng@ipb.pumc.edu.cn (S.C.)

In brief

Gao et al. uncover the structural basis by which RNA anti-CRISPRs (Racrs) inhibit the type I-F CRISPR-Cas system and demonstrate that Racrs competitively divert Cas6f and Cas7f into aberrant assemblies. This sequestration blocks formation of the functional Csy surveillance complex, thereby disabling antiviral defense.

Gao et al., 2026, Molecular Cell *86*, 1–15
January 22, 2026
https://doi.org/10.1016/j.molcel.2025.12.005

CellPress

Please cite this article in press as: Gao et al., RNA anti-CRISPRs deplete Cas proteins to inhibit the CRISPR-Cas system, Molecular Cell (2025), https://doi.org/10.1016/j.molcel.2025.12.005

Molecular Cell

CellPress

Article

RNA anti-CRISPRs deplete Cas proteins to inhibit the CRISPR-Cas system

Xiaopan Gao,[1,2,3,9,*] Kaixiang Zhu,[1,2,3,9] Weihe Zhang,[1,2,3,5,9] Lin Wang,[4,6,9] Linyue Wang,[1,2,3] Lei Hua,[1,2,3,8] Tongxin Niu,[7] Bo Qin,[1,2,3] Xia Yu,[5,*] Hongtao Zhu,[4,6,*] and Sheng Cui[1,2,3,10,*]

[1]NHC Key Laboratory of Systems Biology of Pathogens, National Institute of Pathogen Biology, Chinese Academy of Medical Sciences & Peking Union Medical College, Beijing, China

[2]Key Laboratory of Pathogen Infection Prevention and Control (Ministry of Education), National Institute of Pathogen Biology, Chinese Academy of Medical Sciences & Peking Union Medical College, Beijing, China

[3]State Key Laboratory of Respiratory Health and Multimorbidity, National Institute of Pathogen Biology, Chinese Academy of Medical Sciences & Peking Union Medical College, Beijing, China

[4]Beijing National Laboratory for Condensed Matter Physics, Institute of Physics, Chinese Academy of Sciences, Beijing, China

[5]National Clinical Laboratory on Tuberculosis, Beijing Key laboratory for Drug-resistant Tuberculosis Research, Beijing Chest Hospital, Capital Medical University, Beijing Tuberculosis and Thoracic Tumor Institute, Beijing, China

[6]University of Chinese Academy of Sciences, Beijing, China

[7]Center for Biological Imaging, Institute of Biophysics, Chinese Academy of Sciences, Beijing, China

[8]Yanan medical college of Yanan university, Yanan, China

[9]These authors contributed equally

[10]Lead contact

*Correspondence: gaoxiaopan@pumc.edu.cn (X.G.), yuxia@mail.ccmu.edu.cn (X.Y.), hongtao.zhu@iphy.ac.cn (H.Z.), cui.sheng@ipb.pumc.edu.cn (S.C.)

https://doi.org/10.1016/j.molcel.2025.12.005

SUMMARY

RNA-based anti-CRISPRs (Racrs) interfere with the type I-F CRISPR-Cas system by mimicking the repeats found in CRISPR arrays. Here, we determined the cryo-electron microscopy (cryo-EM) structures of the type I-F crRNA-guided surveillance complex (Csy complex) from *Pectobacterium atrosepticum* and three RacrIF1-induced aberrant subcomplexes. Additionally, we observed that Cas7f proteins could bind to non-specific nucleic acids, forming right-handed superhelical filaments composed of different Cas7 copies. Mechanistically, RacrIF1 lacks the specific S-conformation observed in the corresponding position of the 5′ handle in canonical CRISPR complexes, and it instead adopts a periodic "5 + 1" pattern. This conformation creates severe steric hindrance for Cas5f–Cas8f heterodimer and undermines their binding. Furthermore, Cas7f nonspecifically binds nucleic acids and can form infinite superhelical filaments along Racrs molecules. This oligomerization sequesters Cas6f and Cas7f from binding, therefore blocking the formation of functional CRISPR-Cas effector complexes and ultimately blocking antiviral immunity. Our study provides a structural basis underlying Racrs-mediated CRISPRs inhibition.

INTRODUCTION

The relentless evolutionary arms race between prokaryotes and mobile genetic elements (MGEs) such as phages, plasmids, and transposons has driven the development of diverse and sophisticated defense systems in prokaryotes and viral countermeasures.[1–3] These defense systems include well-characterized restriction-modification (RM) systems,[4] abortive infection mechanisms, newly identified prokaryotic innate immune responses,[3,5–9] and the highly intriguing CRISPR-Cas (clustered regularly interspaced short palindromic repeats; Cas: CRISPR-associated) system.[3,5–8,10–12] CRISPR-Cas systems are prevalent in prokaryotic defense and serve as an adaptive immune system capable of integrating exogenous DNA into the CRISPR locus, thereby storing information of previous viral invasions,[10,13,14] and upon encountering a new invasion, this information is then utilized to specifically silence phages and other MGEs.[10,13,14]

The CRISPR-Cas system generally establishes adaptive immunity through three distinct stages: adaptation, maturation (biogenesis), and interference.[10,15] In the initial phase, short DNA fragments from foreign genetic elements are integrated into the CRISPR array as "spacers," creating a molecular memory of the infection. During the second phase, the CRISPR array is transcribed into a long pre-crRNA, which is subsequently processed by specific ribonucleases into small crRNAs. Each crRNA contains a spacer sequence flanked by a portion of the repeat. In the final phase, a ribonucleoprotein effector complex,

Please cite this article in press as: Gao et al., RNA anti-CRISPRs deplete Cas proteins to inhibit the CRISPR-Cas system, Molecular Cell (2025), https://doi.org/10.1016/j.molcel.2025.12.005

composed of crRNA and Cas proteins, forms crRNA-guided surveillance complexes. These complexes utilize the crRNA as a guide for target recognition and cleavage, effectively neutralizing the invading MGEs.

CRISPR-Cas systems are grouped into two classes (class 1 and class 2), seven types (type I, III, IV, and VII in class 1 and type II, V, and VI in class 2), and more than 30 subtypes based on Cas proteins diversity and interference mechanism.[12,16] The type I system is further divided into seven distinct types including type I A–G. The type I-F CRISPR-Cas system from *Pseudomonas aeruginosa* is extensively characterized structurally and functionally.[17–21] This crRNA-guided surveillance complex comprises nine Cas proteins in a specific stoichiometry: one Cas6f, six Cas7f, one Cas5f, and one Cas8f, accompanied by a single 60-nucleotide crRNA. This complex assembles into an asymmetric spiral architecture. This structural configuration is essential for the stability and function of the surveillance complex. Upon binding to the target DNA, the surveillance complex undergoes a conformational change that facilitates the recruitment of the Cas2/3 helicase-nuclease. The Cas2/3 protein then executes its dual function: unwinding the target DNA helix and introducing cleavage, thereby degrading the invasive genetic material.

To block or circumvent bacterial immunity, phages and/or MGEs developed a variety of protein inhibitors known as anti-CRISPR (Acr) proteins.[22–26] To date, approximately 100 Acr families blocking 12 subtypes of CRISPR-Cas systems have been identified.[27] These Acr proteins employ diverse mechanisms to inhibit CRISPR-Cas activity,[23,25,26,28–30] and the structures of many Acrs bound to the CRISPR-Cas surveillance complex, particularly the type I-F systems, have been determined.[18,26,29–33] Mechanistically, the Acr proteins interfere with the CRISPR-Cas immune response at various stages. They can disrupt Cas–Cas protein interactions, prevent crRNA loading, inhibit the formation of the effector complex, obstruct target DNA binding, and block nuclease recruitment and cleavage.[23,25,28–30,34]

Recent studies have identified CRISPR-like sequences known as solitary repeat units (SRUs) that encode crRNA mimics and function as RNA-based anti-CRISPRs (Racrs).[35,36] Racrs bind Cas proteins to form aberrant CRISPR complexes, thus interfere with the type I-F CRISPR-Cas system, thereby preventing their participation in anti-phage defense. This discovery represents the first paradigm of RNA-based Acrs. However, the high-resolution structural basis underlying how Racrs are recognized by Cas proteins to form these aberrant complexes, and how they undermine functional CRISPR-Cas effector complexes, remains to be elucidated.

In this study, we used cryo-electron microscopy (cryo-EM) to elucidate the molecular mechanism of Racrs-mediated inhibition of CRISPR-Cas immunity.

RESULTS

Overall structure of *P. atrosepticum*-Csy complex

To investigate the structural basis underlying Racrs-based inhibition of CRISPR-Cas immunity, we first purified type I-F (from *Pectobacterium atrosepticum*) cascade bound by crRNA (*P. atrosepticum*-Csy complex). We then determined the cryo-EM structure of *P. atrosepticum*-Csy complex to 2.8 Å (Figures 1A, S1A, S1C, S2A, and S2D; Table S1). The overall architecture of *P. atrosepticum*-Csy complex is a "G"-shaped assembly, in which nine proteins (Cas6f–Cas7f$_{(6x)}$–Cas5f–Cas8f) are skewered by a 60-nt crRNA strand. The complex exhibits several distinct features, including a Cas6f protein at the head capping the 3′ stem-loop of crRNA, a Cas5f–Cas8f heterodimer at the tail capping the 5′ handle of crRNA, and six tandem Cas7f proteins assembled along the crRNA spacer to form a right-handed helical spiral backbone (Figures 1A–1C). Our structure is similar to type I-F *P. aeruginosa*-Csy complex[17,18,21,30] (PDB: 6B45; Figure S3). However, the *P. atrosepticum-Csy* complex exhibits some structural differences compared with other type I-F variant and type I-E cascade complexes[37–40] (Figure S3).

As observed in other class 1 complexes, oligomerization of Cas7f along crRNA induces distortions in its sugar-phosphate backbone due to the thumb domain of Cas7f, creating "kinks" at every 6-nucleotide interval[17,18,41–45] (Figure 1D). In previous cryo-EM structures of the Csy complex, the head region, which includes Cas6f and its capping of the 3′ hairpin of crRNA, was poorly resolved due to inherent flexibility. In contrast, we provide here well-defined density for the entire crRNA region, including the Cas6f subunits. This is evidenced by a significantly improved EM density map of our structure when compared with that of earlier studies (Figures 1E and S4A–S4C), particularly noticeable in the regions where the Cas6f protein interacts with the crRNA (Figure 1E). Notably, the 3′ hairpin of the crRNA in this study appears to be shifted by one base pair compared with previous structures (PDB: 5UZ9 and 6B45) (Figure S4D). While the crRNA structures from the previous studies (PDB: 5UZ9 and 6B45) show good alignment based on the superimposition of the 3′ hairpin of crRNA, our structure exhibits a gradual rigid-body shift throughout the entire crRNA (Figure S4D). However, no clear density is observed for the hook domain of Cas8f. Therefore, we modeled this domain by superposing the Cas8f structure from *P. aeruginosa*-Csy (Figure 1F).

The structures of aberrant Cas subcomplexes

To investigate the aberrant Cas subcomplexes formed by Racrs, we expressed and purified the type I-F *P. atrosepticum*-cascade with RacrIF1 as previously described (Figure 2A).[35] Consistent with previous findings, we successfully obtained and solved the structure of an aberrant Cas subcomplex containing only Cas6f, Cas7f, and RacrIF1, but lacking both Cas5f and Cas8f.[35] During particle analysis, we identified three distinct populations, each comprising one Cas6f protein bound to a RacrIF1 RNA, with varying numbers of Cas7f proteins: the first containing seven Cas7f subunits (confor-1), the second containing eight Cas7f subunits (confor-2), and the third containing nine Cas7f subunits (confor-3) with the dominant particle fraction (Figures 2B and 2C). The confor-1 and confor-2 classes likely represent on-pathway intermediates captured during vitrification, corresponding to intermediate assembly states in a sequential Cas7f-addition pathway. The 3D reconstruction of confor-3 yielded enhanced density with an improved resolution of 2.8 Å (Figure S5B; Table S1). Therefore, the confor-3 reconstruction was used for atomic model building (Figure 2C).

Please cite this article in press as: Gao et al., RNA anti-CRISPRs deplete Cas proteins to inhibit the CRISPR-Cas system, Molecular Cell (2025), https://doi.org/10.1016/j.molcel.2025.12.005

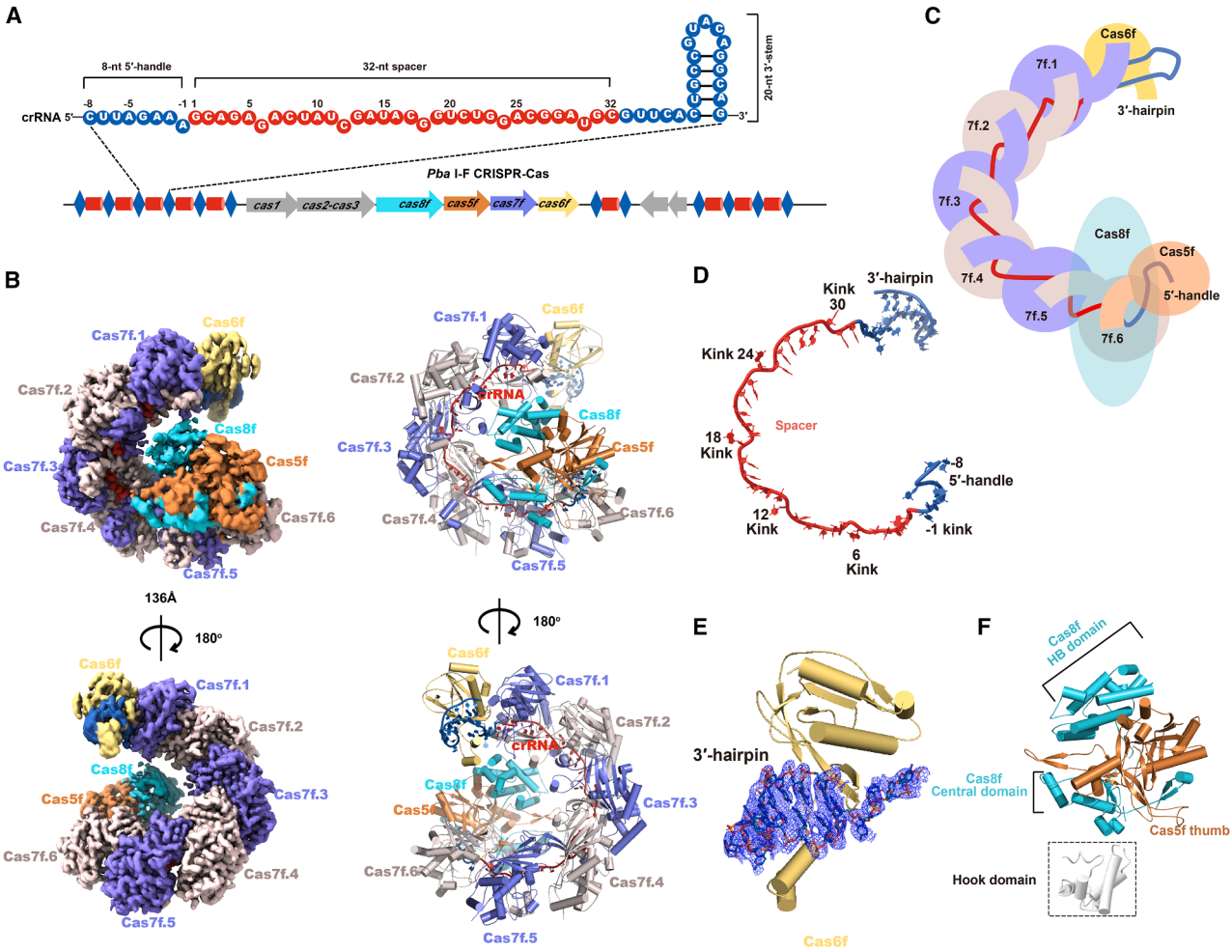

Figure 1. Cryo-EM structure of the type I-F *Pba*-Csy complex

(A) Schematic representation of the type I-F CRISPR-Cas locus from *P. aterosepticum* (Pba). The crRNA is shown with the 8-nt 5′ handle (blue), 32-nt spacer (red), and 3′ stem-loop (blue). The Cas genes are consecutively arranged in the genome and labeled with their respective names along the CRISPR array.

(B) Cryo-EM structure of the *Pba*-Csy complex. Two views are presented with a 180° rotation. The complex is composed of one Cas6f, one Cas5f, one Cas8f, and six Cas7f proteins, with crRNA tethering the nine Cas protein subunits together. Each subunit is labeled and color-coded consistently with (A).

(C) Simplified diagram of the *Pba*-Csy complex illustrating the "G" shaped architecture. The Cas6f protein caps the 3′ hairpin, Cas5f-Cas8f heterodimer caps the 5′ handle, and the Cas7f proteins form a helical backbone along the crRNA spacer.

(D) The crRNA spacer showing the "kinks" induced by the Cas7f proteins at every 6-nucleotide interval. Specific kinks at nucleotide positions −1, 6, 12, 18, 24, and 30 are highlighted.

(E) Close-up view of the Cas6f interaction with the 3′ hairpin of the crRNA, showing well-defined density for the 3′ hairpin region of crRNA.

(F) Model of the hook domain (dashed box) of *Pba*-Cas8f based on the superimposition of the Cas8f structure from the *P. aeruginosa*-Csy complex. The Cas8f central domain, the helical bundle (HB) domain and Cas5f thumb domain of *Pba*-Csy complex are indicated.

Unlike the *P. atrosepticum*-Csy complex, RacrIF1-induced aberrant subcomplexes consist of seven to nine Cas7f proteins that oligomerize along the RacrIF1, forming a helical filament along its length. This oligomerization transforms the original "G" shape into either a "C" shape (confor-1) or an "S" shape (confor-3) (Figures 2B and 2C). We modeled 69 nucleotides of RacrIF1, including 32 nucleotides for pseudo-spacer (denoted pseudo-spacer here to distinguish it from crRNA spacer), 20 nucleotides for 3′-hairpin, and the 17 nucleotides for 5′-handle variant (denoted 5′-handle variant to distinguish it from the crRNA 5′-handle) (Figures 2A and 2D). Similar to the binding mode of six Cas7f proteins to crRNA, Cas7f proteins also oligomerize along RacrIF1, introducing deformations in the sugar-phosphate backbone, and resulting in kinks at regular six-nucleotide intervals (Figure 2D). However, due to the presence of the 5′-handle variant, Cas7f.7 continues to oligomerize along RacrIF1 toward its 5′ direction, the remaining six nucleotides are ordered across the web domain of the next Cas7 subunit. Cas7f.8 binds subsequent RNA in the same manner, ultimately dividing the RacrIF1-guide sequence in eight discrete segments (Figure 2D). At positions −13, −7, −1, 6, 12, 18, 24, and 30 of each segment, a nucleotide base is buried through interactions

Please cite this article in press as: Gao et al., RNA anti-CRISPRs deplete Cas proteins to inhibit the CRISPR-Cas system, Molecular Cell (2025), https://doi.org/10.1016/j.molcel.2025.12.005

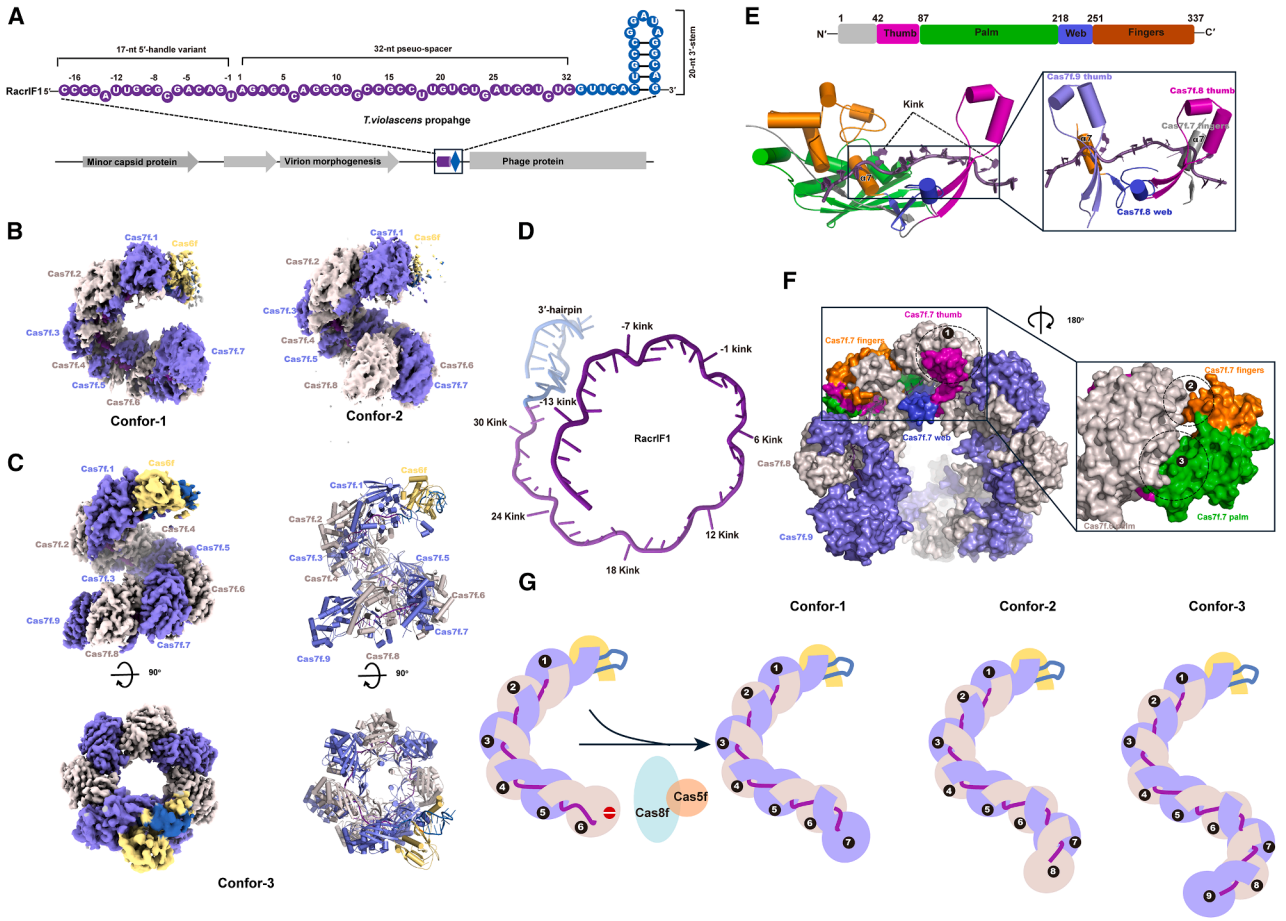

Figure 2. Cryo-EM structure of the aberrant Cas subcomplexes

(A) Schematic representation of the RacrIF1 sequence from the *T. violascens* prophage, highlighting its secondary structure elements: the 17-nucleotide 5′ handle variant, the 32-nucleotide spacer, and the 20-nucleotide 3′ hairpin sequence.

(B) Cryo-EM maps of confor-1 and confor-2 showing the arrangement of Cas7f subunits. In confor-1, seven Cas7f subunits are visualized, while confor-2 displays the addition of an eighth Cas7f subunit. The Cas6f subunit and the 3′ hairpin are poorly resolved in these maps.

(C) Cryo-EM reconstruction of confor-3, displaying the stable assembly of nine Cas7f subunits. The different orientations provide a comprehensive view of the complex architecture. The Cas6f subunit and the 3′ hairpin are partially resolved in this map.

(D) Topological representation of the RacrIF1 structure, indicating the locations of kinks at regular six-nucleotide intervals. Each segment buries a nucleobase of RacrIF1 at positions −13, −7, −1, 6, 12, 18, 24, and 30.

(E) Upper: the Cas7f domain organization is depicted with different colors. The thumb domain is colored magenta, the palm domain green, the web domain blue, and the fingers domain orange. Lower: one RacrIF1 segment interacts with the Cas7f fingers, palm, web, and thumb, colored as in the upper panel. The inset shows the interaction between the thumb of Cas7f.9 (lavender), the web (blue), and α7 (orange) of Cas7f.8, and the α7 (gray) of Cas7f.7.

(F) Surface representation of the Cas7f spatial arrangement of the subunits. The inset provides a zoomed-in view of the interaction between Cas7f-6 and Cas7f-7. Three interaction interfaces are indicated.

(G) Proposed model for the assembly of aberrant Cas subcomplexes.

with three consecutive Cas7 copies (e.g., Cas7f.7, Cas7f.8, and Cas7f.9) (Figures 2D and 2E). The structure of a single Cas7f molecule resembles a "right hand," comprising distinct domains: the fingers (residues 251–337), the palm (residues 87–217), the thumb (residues 42–86), and a web domain loop (residues 218–250) interspersed between the fingers and thumb (Figures 2E and S6). The interactions with the phosphate backbone of each RacrIF1 segment are primarily mediated by the two α7 helices from neighboring Cas7f subunits, along with the web and thumb regions (Figure 2E).

Three interfaces mediate interactions between Cas7f.7 and Cas7f.6 (Figure 2F). The first interface is formed between the tip of the thumb of the Cas7f.7 subunit and the fingers of the neighboring Cas7f.6 subunit (❶). The second interface is formed between the fingers of the Cas7f.7 subunit and the back of the palm of the neighboring Cas7f.6 subunit (❷). The third interface is formed between the palm of the Cas7f.7 subunit and the front of the palm of the neighboring Cas7f.6 subunit (❸) (Figure 2F). The conformations between Cas7f.4–6 and Cas7f.7–9 are essentially identical (Figure S7A).

Please cite this article in press as: Gao et al., RNA anti-CRISPRs deplete Cas proteins to inhibit the CRISPR-Cas system, Molecular Cell (2025), https://doi.org/10.1016/j.molcel.2025.12.005

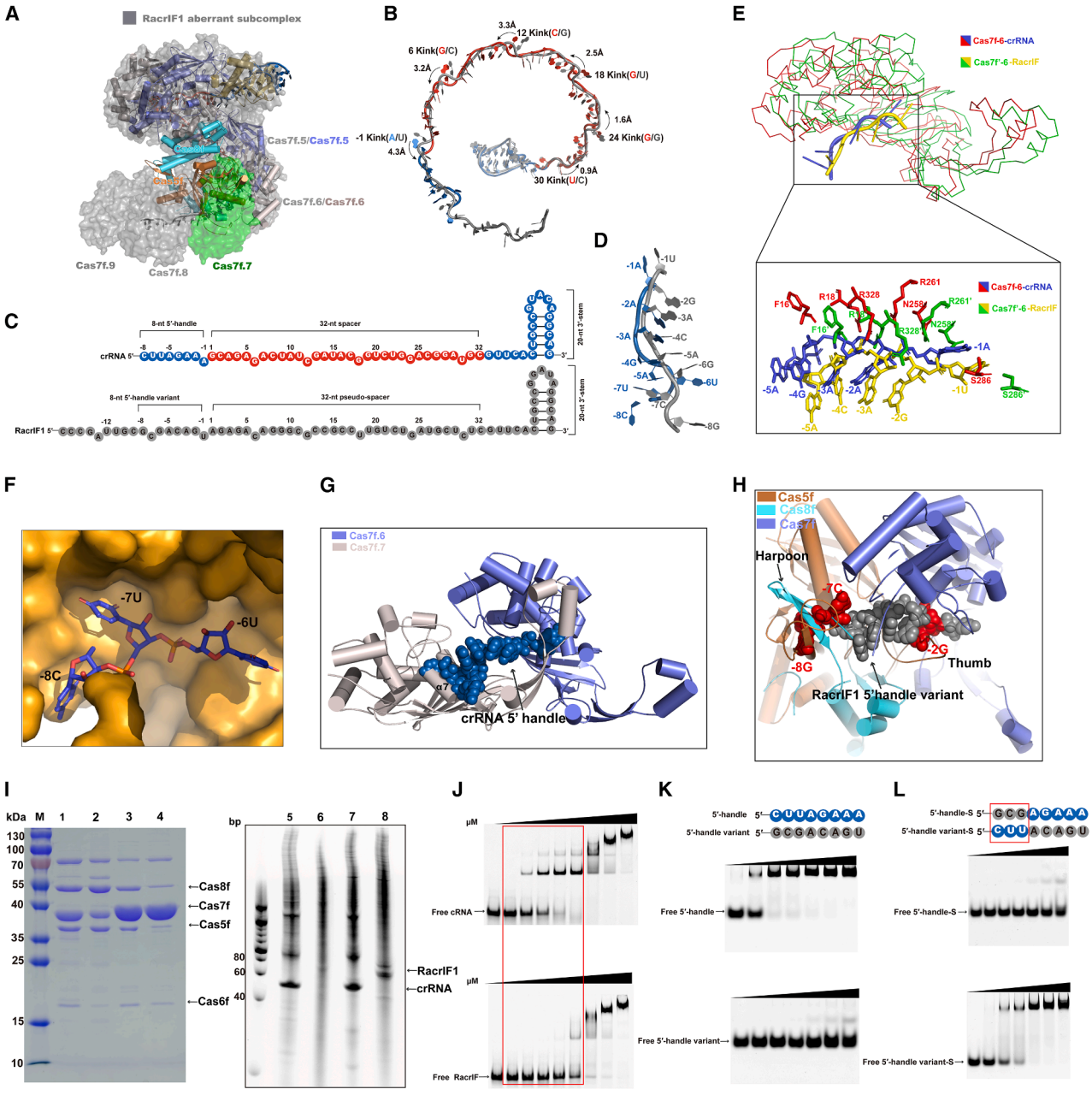

Figure 3. Structural and functional analysis of RacrIF1 inhibition on the *Pba*-Csy complex

(A) Superimposition of the *Pba*-Csy complex with the aberrant Cas subcomplexes indicates that Cas7f.5 and Cas7f.6 subunits align well, but Cas5f (orange) from the *Pba*-Csy complex clashes severely with Cas7f.7 (green) from the aberrant Cas subcomplexes, suggesting spatial incompatibility. The aberrant Cas subcomplexes are presented as a surface model, while the *Pba*-Csy complex is presented as a cartoon model.

(B) Superimposition of crRNA with RacrIF1 reveals slight rigid body movements of RacrIF1. The kinks and shifts in angstroms (Å) at positions 30, 24, 18, 12, 6, and −1 are indicated, showing a gradual increase in displacement from 0.9 Å at position 30 to 4.3 Å at position −1. These movements are highlighted with black arrows showing the degrees of displacement.

(C) Comparison of the secondary structure sequences of crRNA and RacrIF1 indicates a high degree of similarity. crRNA is colored the same as in Figure 1A, and RacrIF1 is colored in gray.

(D) Comparison of the tertiary structures of the 5′ handle of crRNA and the 5′ handle variant region of RacrIF1 reveals highly similar orientations for the first five bases, despite an overall positional shift. The 5′ handle is colored blue, and the 5′ handle variant is colored gray. The nucleotide numbers are labeled.

(E) Upper: superimposition of the 5′ handle of crRNA and Cas7f.6 in the *Pba*-Csy complex with the 5′ handle variant of RacrIF1 and Cas7f′.6 in the aberrant Cas subcomplexes. Lower: a zoomed-in view of the superimposition of residues interacting with the 5′ handle of crRNA from Cas7f.6 in the *Pba*-Csy complex and the 5′ handle variant of RacrIF1 from Cas7f′.6 in the aberrant Cas subcomplexes. The Cas7f.6 and crRNA are colored red and blue, respectively, while the Cas7f′.6

(legend continued on next page)

Please cite this article in press as: Gao et al., RNA anti-CRISPRs deplete Cas proteins to inhibit the CRISPR-Cas system, Molecular Cell (2025), https://doi.org/10.1016/j.molcel.2025.12.005

In summary, we propose a model for the assembly of aberrant Cas subcomplexes induced by RacrIF1 (Figure 2G). Initially, the first six Cas7f subunits bind to RacrIF1 similarly to their interaction with crRNA. However, the absence of a canonical 5′ handle prevents the recruitment of Cas5f and Cas8f heterodimer, resulting in Cas7f oligomerization along the 5′ portion of RacrIF1. This oligomerization continues, ultimately leading to the formation of stable complexes containing seven to nine Cas7f subunits.

RacrIF1 5′-handle variant induce aberrant Cas subcomplexes

To further elucidate the mechanism of the RacrIF1-mediated inhibition on functional *P. atrosepticum*-Csy complex, we individually defined the principal axis of the *P. atrosepticum*-Csy complex and the aberrant Cas subcomplexes. The *P. atrosepticum*-Csy complex exhibits a compact conformation with a principal axis length of 115 Å and a diameter of 140 Å (Figure S7B). In contrast, the aberrant Cas subcomplexes display an expanded conformation with a principal axis length of 142 Å and a diameter of 134 Å (Figure S7C). This indicates that, while the diameters of the *P. atrosepticum*-Csy complex and aberrant Cas subcomplexes are similar, their principal axis lengths are remarkably different. This difference is primarily attributed to the addition of three Cas7f subunits to the aberrant Cas subcomplexes, which extends their length (Figure 2C). Superimposition of the *P. atrosepticum*-Csy complex with the aberrant Cas subcomplexes shows that the subunits Cas7f.5 and Cas7f.6 align well between the two structures. However, Cas5f from the *Pba*-Csy complex severely clashes with Cas7f.7 from the aberrant Cas subcomplexes, indicating that Cas5f and Cas7f.7 subunits cannot coexist in the same spatial arrangement (Figure 3A). Superimposition of crRNA with RacrIF1 reveals significant rigid-body movements of RacrIF1, with the pseudo-spacer sequence displacement gradually increasing from 0.9 Å at the flipped base position 30 to 4.3 Å at the flipped base position −1 (Figure 3B). Comparison of the secondary structure sequences of crRNA and RacrIF1 indicates a high degree of similarity (Figure 3C). Examination of the tertiary structures of the 5′ handle of crRNA and the 5′ handle variant region of RacrIF1 reveals that the first five bases, despite an overall positional shift, exhibit highly similar conformation (Figure 3D). Additionally, the orientations of the amino acids in Cas7f.6 from the *Pba*-Csy complex and Cas7f′.6 from the aberrant Cas subcomplexes, which interact with the 5′ handle of crRNA and the 5′ handle variant of RacrIF1, via sequence non-specific interaction, are similar (Figure 3E). This suggests that the binding pattern of the first five bases (from −1 to −5) in the crRNA 5′ handle, and the RacrIF1 5′ handle variant, is highly conserved (Figure 3E). However, the last three nucleotides (−8C, −7U, and −6U) in the crRNA 5′ handle are splayed and fitted into base-specific binding pockets formed by Cas5f (Figure 3F). In contrast, the last three nucleotides (−8G, −7C, and −6G) in the RacrIF1 5′ handle variant remain ordered, continuing across the α7 helices and the thumb of the next subunit via sugar-phosphate backbone-mediated, non-specific interactions (Figure 2E).

To further understand why the 5′ handle is specific to the *Pba*-Csy complex, whereas the 5′ handle variant is preferred by aberrant Cas subcomplexes, we modeled the 5′ handle into the corresponding position of the 5′ handle variant in Cas7f.6 and Cas7f.7 within the aberrant Cas subcomplexes. The last three nucleotides (−8C, −7U, and −6U) in the crRNA 5′ handle clash severely with the Cas7f.7 subunit (Figure 3G). Similarly, when modeling the 5′ handle variant into the corresponding position of the 5′ handle in Cas5f and Cas8f within the *Pba*-Csy complex, the last two nucleotides (−8G and −7C) in the RacrIF1 5′ handle variant clash severely with the Cas5f and the harpoon of the Cas8f subunit (Figure 3H). Therefore, the RacrIF1 5′ handle variant is disfavored for Cas5f-Cas8f binding but preferred

and RacrIF1 are colored green and yellow. The binding residues for the first five bases (from −1 to −5) in both the crRNA 5′ handle and the RacrIF1 5′ handle variant are shown as stick models and labeled.

(F) Cas5f is presented as a surface model, with the last three nucleotides (−8C, −7U, and −6U) in the crRNA 5′ handle shown as stick models. These three nucleotides are splayed and fitted into base-specific binding pockets formed by Cas5f.

(G) Modeling the 5′ handle into the corresponding position of the 5′ handle variant in Cas7f.6 and Cas7f.7 within the aberrant Cas subcomplexes. The Cas7f.6 and Cas7f.7 subunits are shown as cartoon models, while the crRNA 5′ handle is depicted as a spheres model.

(H) Modeling the 5′ handle variant into the corresponding position of the 5′ handle in Cas5f and Cas8f within the *Pba*-Csy complex. The Cas5f, the harpoon of the Cas8f subunit, and Cas7f are shown as cartoon models, while the RacrIF1 5′ handle variant is depicted as a sphere model.

(I) Left: SDS-PAGE gel showing the His-tag pull-down assay. (1) The elution of Cas6f, Cas7f, Cas5f, and Cas8f when the Cas5f-Cas8f heterodimer with a His-tag added to Cas8f was co-expressed with Cas6f and Cas7f along with crRNA. (2) The elution of Cas6f, Cas7f, Cas5f, and Cas8f when the Cas5f-Cas8f heterodimer with a His-tag added to Cas8f was co-expressed with Cas6f and Cas7f along with RacrIF1. The elution of Cas5f and Cas8f in the presence of RacrIF1 was more evident than with crRNA, while the elution of Cas7f was less evident. (3) The elution of Cas6f, Cas7f, Cas5f, and Cas8f when Cas6f with a His-tag added to Cas7f was co-expressed with Cas5f and Cas8f along with crRNA. (4) The elution of Cas6f, Cas7f, Cas5f, and Cas8f when Cas6f with a His-tag added to Cas7f was co-expressed with Cas5f and Cas8f along with RacrIF1. The elution of Cas5f and Cas8f in the presence of RacrIF1 was almost undetectable, while the elution of Cas7f was comparable to crRNA. Right: corresponding RNAs extracted from the same purified complexes and visualized by SYBR gold staining. The RNA gel is presented alongside the SDS-PAGE protein gel to allow direct comparison of protein and RNA components within each complex, thereby facilitating interpretation of RNA-protein associations.

(J) EMSA demonstrating the binding affinity of the Cas5f-Cas8f heterodimer to crRNA or RacrIF1. The differences in binding affinity are outlined in a red box. Cas5f-Cas8f was titrated at concentrations of 0.2–8 μM against a fixed crRNA/RacrIF1 concentration of 0.25 μM.

(K) EMSA demonstrating the binding affinity of the Cas5f-Cas8f heterodimer to the 5′ handle and 5′ handle variant. The sequence of the 5′ handle and 5′ handle variant are displayed, with nucleotides color-coded in blue and gray, respectively. Cas5f-Cas8f was titrated at concentrations of 0.2–8 μM against a fixed RNA concentration of 0.25 μM, as in (J).

(L) EMSA demonstrating the binding affinity of the Cas5f-Cas8f heterodimer to the 5′ handle S (where the last three nucleotides in the 5′ handle were swapped with the corresponding nucleotides from the 5′ handle variant) and 5′ handle variant S (where the last three nucleotides in the 5′ handle variant were swapped with the corresponding nucleotides from the 5′ handle). The swapped nucleotides are outlined in a red box. The concentrations of Cas5f-Cas8f and RNA used in this assay are identical to those described in (J).

Please cite this article in press as: Gao et al., RNA anti-CRISPRs deplete Cas proteins to inhibit the CRISPR-Cas system, Molecular Cell (2025), https://doi.org/10.1016/j.molcel.2025.12.005

by Cas7f, thus leading to the formation of aberrant Cas subcomplexes.

Our structural analysis was confirmed by a His-tag pull-down assay. When the Cas5f–Cas8f heterodimer, with a His-tag added to Cas8f, was co-expressed with Cas6f and Cas7f together with crRNA and RacrIF1, the His-tag-pull-down elution of Cas5f and Cas8f in the presence of RacrIF1 was even more prominent than that observed with crRNA, whereas the elution of Cas7f was less pronounced compared with the crRNA condition (Figure 3I; lane 2). The corresponding RNA gels showed that a substantial amount of crRNA was also pulled down, whereas only a trace amount of RacrIF1 was detected (Figure 3I; lane 5). This result explains why the elution of Cas7f was less evident in the presence of RacrIF1 than with crRNA. Conversely, when Cas6f, with a His-tag added to Cas7f, was co-expressed with Cas5f and Cas8f together with crRNA and RacrIF1, the His-pull-down elution of Cas5f and Cas8f in the presence of RacrIF1 was significantly reduced, while the elution of Cas7f remained comparable to that with crRNA (Figure 3I; lane 4). The corresponding RNA gels showed nearly equal amounts of crRNA and RacrIF1 RNA (Figure 3I, lane 8); however, the Cas5f–Cas8f signal was markedly decreased, further supporting that RacrIF1 interferes with their binding (Figure 3I, lane 4).

The electrophoretic mobility shift assay (EMSA) further demonstrates that the binding affinity of the Cas5f–Cas8f heterodimer to crRNA or the 5′ handle is significantly stronger than to RacrIF1 and the 5′ handle variant (Figures 3J and 3K). The 5′ handle variant almost completely loses its binding affinity to the Cas5f–Cas8f heterodimer (Figure 3K). Notably, when the last three nucleotides of the 5′ handle variant were replaced with the corresponding nucleotides from the 5′ handle (named 5′ handle variant-S), its binding affinity to the Cas5f–Cas8f heterodimer improved significantly, becoming comparable to that of the 5′ handle (Figure 3L). Conversely, when the last three nucleotides of the 5′ handle are swapped with the corresponding nucleotides from the 5′ variant (denoted as 5′ handle -S), its binding affinity significantly decreases, resulting in almost no binding to Cas5f-Cas8f heterodimer (Figure 3L).

To further investigate the impact of alternative sequences in the 5′ handle on the binding affinity to the Cas5f–Cas8f heterodimer, we synthesized various 5′ handle variants and conducted EMSA experiments. When the last three nucleotides, CUU, were kept unchanged and the remaining five nucleotides of the 5′ handle were randomized (named CUU1 and CUU2), the binding affinity was nearly identical to that of the wild-type 5′ handle (Figure S7D). However, when the last three nucleotides of the 5′ handle were randomized, while the remaining five nucleotides were fixed (named AGAAA1 and AGAAA2), the binding affinity was significantly reduced, with the AGAAA2 variant nearly losing its ability to bind to the Cas5f–Cas8f heterodimer (Figure 7E). Furthermore, when the entire 5′ handle sequence was randomized–meaning both the last three nucleotides and the remaining five nucleotides were altered–both variants lost their ability to bind to the Cas5f–Cas8f heterodimer (Figure S7F).

These results further confirm that the CUU sequence plays an essential role in specific binding, acting as a key determinant for the interaction with the Cas5f–Cas8f heterodimer, while the AGAAA sequence contributes minimally, primarily facilitating non-specific binding. Additionally, we synthesized 5′ handle sequences from type I-F CRISPR-Cas system crRNAs derived from different sources, including *P. aeruginosa* (PDB: 6B45) and *Vibrio* phage ICP1_2011 (PDB: 7WWU). These sequences are highly conserved, particularly the CUU sequence at positions from −8 to −5. As anticipated, their binding affinity for the Cas5f–Cas8f heterodimer was comparable to that of the 5′ handle crRNAs from *P. atrosepticum* (Figure S7G).

Competitive mechanism between Csy and RacrIF1-induced aberrant complexes

To directly test whether Racrs can cause the disassembly of the pre-assembled Csy complex, we purified and assembled the *Pba*-Csy complex, which was subsequently concentrated and incubated with RacrIF1 at a 1:3 molar ratio *in vitro*, followed by further purification using gel filtration chromatography. Urea-PAGE analysis showed no detectable incorporation of RacrIF1 into the Csy complex (Figure 4A). Consistently, SDS-PAGE analysis revealed that the protein composition of the pre-assembled Csy complex remained unchanged following RacrIF1 addition, indicating that RacrIF1 does not disassemble the pre-formed complex (Figure 4A). Together, these results demonstrate that Racrs cannot disrupt assembled surveillance complexes. In contrast, Racrs inhibit CRISPR-Cas function by competing with crRNAs for shared Cas components during complex assembly, thereby shifting the equilibrium between functional and aberrant complexes and ultimately preventing the formation of active surveillance complexes. To test this model, we co-expressed the Csy functional complex and the Racrs-induced aberrant complex using three separate plasmids (*pQE60-cas8f-cas5f-His-cas7f*, *pRSFDuet-cas6f-RacrIF1*, and *pACYCDuet-crRNA*), allowing RacrIF1 and crRNA to compete for Cas proteins during the assembly process. The purified sample contained both the functional and aberrant Csy complexes, which could not be fully resolved by gel filtration chromatography (Figure 4B). Nucleic acid gel analysis revealed the presence of both crRNA and RacrIF1 within the same preparation, indicating that the functional and aberrant complexes coexisted in the purified mixture (Figure 4B). These results provide strong evidence for a competition-based mechanism in which Racrs and crRNAs assemble with the same pools of Cas proteins.

To directly assess whether Racrs are capable of inactivating the assembled CRISPR complex, we performed nuclease activity assay using double-stranded DNA (dsDNA) bubble substrates, following the approach established previously.[46] As expected, the Cas1-2/3 complex alone exhibited no DNA cleavage activity, consistent with Cas1-mediated inhibition of Cas2/3 nuclease activity (Figure 4C). Addition of the functional Csy complex restored cleavage of the bubbled DNA substrate, confirming that DNA-bound Csy activates the Cas1-2/3 nuclease (Figure 4C), as reported earlier,[46] whereas the Racrs-induced aberrant complex lacks DNA cleavage activity, confirming its non-functional state (Figure 4C). Consistent with our previous observation that Racrs do not dismantle preassembled surveillance complexes, RacrIF1 did not inhibit the nuclease activity of the fully formed functional Csy complex (Figure 4D). However, mixtures derived from the co-expression of the Csy functional complex and the Racrs-induced aberrant complex (containing

Please cite this article in press as: Gao et al., RNA anti-CRISPRs deplete Cas proteins to inhibit the CRISPR-Cas system, Molecular Cell (2025), https://doi.org/10.1016/j.molcel.2025.12.005

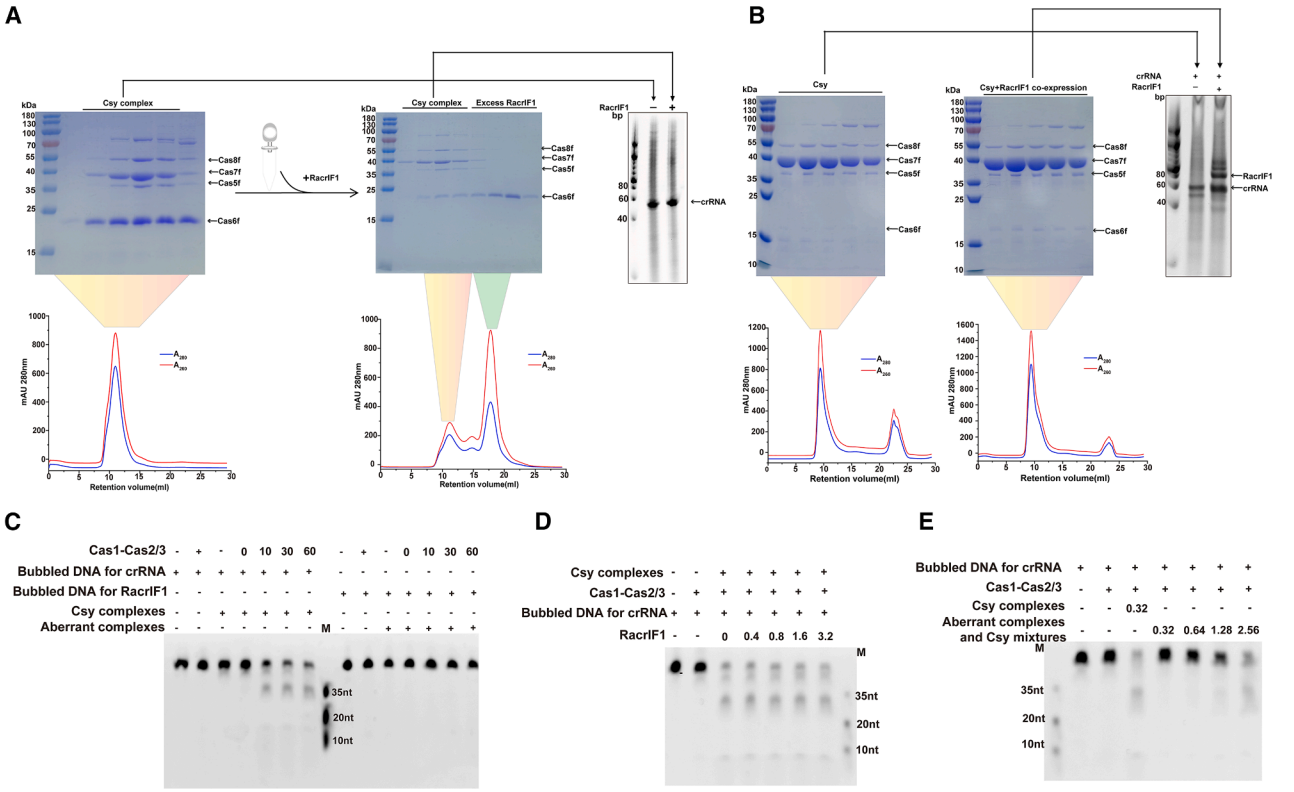

Figure 4. *In vitro* assembly and *in vivo* co-expression analyses reveal the competitive mechanism between Csy and RacrIF1-induced aberrant complexes

(A) The preassembled Csy complex (left) was incubated with an excess of RacrIF1 RNA (1:3 molar ratio) and reanalyzed by gel filtration chromatography (middle). The chromatogram (middle) shows two distinct peaks, corresponding to the intact Csy complex and the separately eluting RacrIF1 RNA. SDS-PAGE (middle) of the peak fractions confirms that RacrIF1 does not disassemble the preformed Csy complex. Nucleic acid gel analysis (right) confirms that RacrIF1 is absent from the Csy complex.

(B) Co-expression of RacrIF1 with the Csy subunits resulted in the formation of both functional and aberrant Csy complexes. The purified sample contained a mixture of these assemblies, which could not be completely separated by gel filtration chromatography. Nucleic acid gel (right) analysis revealed the coexistence of crRNA and RacrIF1 within the same preparation, confirming that both functional and aberrant Csy complexes were present in the purified mixture.

(C) Nuclease activity assays were performed using bubbled dsDNA substrates for crRNA and RacrIF1. Purified Cas1-Cas2/3 (0.5 μM) complexes were incubated with the indicated DNA substrates (0.04 μM) in the presence or absence of the functional or aberrant Csy complexes (0.32 μM) for the indicated times (0, 10, 30, and 60 min). Reaction products were analyzed by urea-PAGE and visualized by fluorescence imaging.

(D) Nuclease activity assays of the functional Csy complex (0.32 μM) in the presence of increasing concentrations of RacrIF1 (0–3.2 μM). Cas1-Cas2/3 (0.5 μM) and bubbled DNA substrates (0.04 μM) were included and indicated in all reactions. Reaction products were analyzed by urea-PAGE and visualized by fluorescence imaging.

(E) Nuclease activity assays using mixtures containing both of functional and aberrant Csy complexes (0.32–2.56 μM). Cas1-Cas2/3 (0.5 μM) and bubbled DNA substrates (0.04 μM) for crRNA were included in all reactions. Reaction products were resolved by urea-PAGE and visualized by fluorescence imaging.

both functional and aberrant Csy assemblies) exhibited a pronounced reduction in DNA cleavage activity. Only when the total complex concentration was increased to approximately 10-fold higher than that of the functional Csy complex alone did we observe a comparable level of nuclease activity (Figure 4E). These findings demonstrate that co-expression of Racrs markedly inhibits CRISPR-Cas function *in vitro* by competitively sequestering essential Csy components *in vivo*.

Collectively, our results demonstrate that RacrIF1 preferentially binds to Cas7f rather than the Cas5f–Cas8f heterodimer due to 5′ handle variant, thereby yielding the aberrant Cas subcomplexes. These findings support a competition-based mechanism in which Racrs and crRNAs assemble using the same pools of Cas proteins. In addition, our structural and biochemical data explain why Racrs-induced complexes fail to support primed adaptation, as reported previously.[35] RacrIF1 forms an aberrant Csy subcomplex lacking Cas5f–Cas8f, which is required for DNA targeting and recruitment of the Cas1-Cas2/3 adaptation module. Consequently, these defective assemblies are unable to activate Cas2/3 or mediate spacer acquisition, explaining the loss of primed adaptation in Racrs-expressing cells.

Architecture of Cas7f filament assembly

During 2D classification, we observed a subset of particles forming superhelical solenoid structures in samples expressing type I-F *Pba*-cascade with RacrIF1 (Figure S5). Through 3D

Please cite this article in press as: Gao et al., RNA anti-CRISPRs deplete Cas proteins to inhibit the CRISPR-Cas system, Molecular Cell (2025), https://doi.org/10.1016/j.molcel.2025.12.005

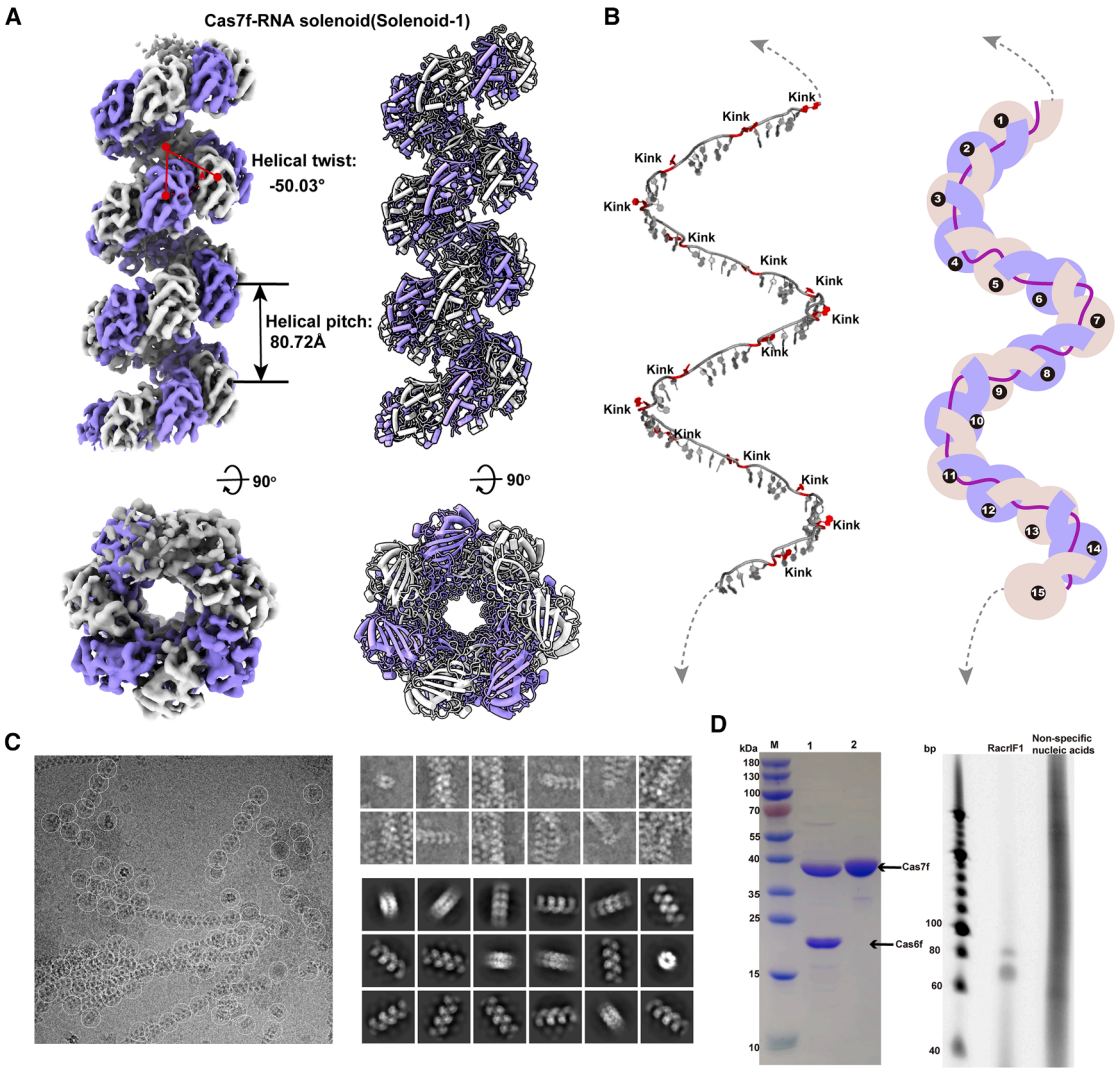

Figure 5. The architecture Cas7f filament assembly

(A) Density maps and fitted models of solenoid-1 viewed from different angles (90° and top views). The refined helical parameters are a twist of −50.03° and a pitch of 80.72 Å, corresponding to the periodic rise and rotation between adjacent Cas7f subunits. Cas7f subunits are alternately colored blue and white, and nucleic acids are depicted in gray.

(B) Left: schematic representation of the random sequence of the nucleic acids within the solenoid formed by Cas7f subunits. The kinks and flipped nucleotide (colored by red) are indicated. Right: model showing the helical arrangement of Cas7f subunits (alternating blue and light pink) along the nucleic acid strand (pink). The numbers indicate the sequential arrangement of Cas7f subunits.

(C) Cryo-EM micrographs and 2D class averages of Cas7f-RacrIF1 sample filaments. Left: a representative cryo-EM micrograph. Right: various 2D class averages of Cas7f-RacrIF1 filaments.

(D) Left: SDS-PAGE of co-expression of Cas6f, RacrIF1, and Cas7f (lane 1), the co-expression of Cas7f and RacrIF1 (lane 2). Right: urea-PAGE of the same samples as shown in the SDS-PAGE. The smear band indicating the presence of non-specific nucleic acids and the absence of RacrIF1.

reconstruction, we revealed that these helical tubing structures were constituted by numerous Cas7f copies. To enhance the overall resolution and structural consistency, helical symmetry was imposed during the reconstruction, as detailed in the STAR Methods section, and we termed this Cas7f-RNA solenoid (solenoid-1) conformation (Figure 5A). Using Chimera, we modeled Cas7f subunits and random nucleic acids for rigid-body fitting, and the fitted model was then refined as described in the STAR Methods (Figure 5B). The random nucleic acids adopted a conformation similar to confor-3, as described in The structures of aberrant Cas subcomplexes (Figure 2), with Cas7f subunits oligomerizing along the nucleic acid. These subunits extend from an initial nine-subunit assembly into an effectively infinite filament (Figure 5B). Notably, despite performing focused classification on the ends of the filament, we did not observe any density corresponding to Cas6f or the 3′ stem loop. The helical tubes have infinite ends extending toward both directions with Cas7f copies only.

Please cite this article in press as: Gao et al., RNA anti-CRISPRs deplete Cas proteins to inhibit the CRISPR-Cas system, Molecular Cell (2025), https://doi.org/10.1016/j.molcel.2025.12.005

To further confirm this finding, we designed a construct expressing only Cas6f, RacrIF1, and Cas7f (Figures S1B and S1C). Cryo-EM analysis of this construct sample also revealed helical tube conformations consisting solely of Cas7f, without density for Cas6f in our 3D reconstruction (solenoid-2) (Figures S2B, S2E, and S8A). To compare the structural organization of the two solenoids, we superimposed the solenoid-2 and solenoid-1 models. The overlay revealed a nearly identical helical arrangement between the two assemblies, demonstrating a high degree of structural similarity and conservation in their overall helical organization (Figure S8A). This suggests that Cas7f independently binds to nucleic acids without the involvement of Cas6f, and the bound nucleic acids are likely non-specific rather than RacrIF1.

To test this hypothesis, we expressed Cas7f and RacrIF1 and subjected the samples to cryo-EM analysis. Micrograph analysis revealed that a significant fraction of Cas7f–RacrIF1 particles exhibited filament-like assemblies (Figure 5C). 2D classification of these filaments revealed varying segments similar to the solenoid-1 and solenoid-2, here named Cas7f-RNA solenoid (solenoid-3) (Figures S2C and S2F). When performing rigid-body fitting of the solenoid-1 model into the EM density of solenoid-3, the positions of the model aligned well with the solenoid-3 density (Figure S8B).

Our analysis confirmed that the three helical tube conformations were likely formed by Cas7f with non-specific nucleic acids, without the involvement of Cas6f. This hypothesis was further validated by urea-PAGE analysis, which revealed that the Cas7f-RacrIF1 sample did not contain RacrIF1, but instead exhibited a smear band indicative of a large amount of non-specific nucleic acids (Figure 5D). This observation is consistent with previous studies showing that Csy3 (Cas7f), or Csy3 co-expressed with mutant Csy4 (Cas6f) along with crRNA, purifies as a large oligomeric complex containing non-specific RNA.[47]

To further demonstrate that Cas6f-mediated cleavage is highly conserved and essential for the assembly of both the crRNA-guided surveillance complex (Csy complex) and RacrIF1-induced aberrant subcomplexes, we analyzed the Cas6f-RNA interface in detail. Building upon the observed structural similarity, sequence conservation, and prior functional validation of key residues involved in crRNA recognition[47–49] (Figures S9A and S9B), we investigated how Cas6f engages with the 3′ hairpin of crRNA or RacrIF1 (Figures S9C–S9J). Specifically, an arginine-rich α helix of Cas6f inserts into the major groove of the hairpin stem, forming an extensive hydrogen bond network with the phosphate backbone of the 5′ strand through multiple arginine residues (R108 and R111), while the side chain of Arg112 forms a specific hydrogen bond with the base of G11. In addition, Cas6f recognizes the two terminal base pairs of the stem-loop via a direct readout mechanism, forming base-specific hydrogen bonds between the major groove faces of A19 and G20 and the side chains of Gln101 and Arg99, respectively. The aromatic side chain of Phe152 stacks beneath the terminal base pair, thereby stabilizing the local conformation and positioning the scissile phosphate within the active site. Following cleavage, the resulting phosphate group forms hydrogen bonds with the side chain of His29. Furthermore, the ribose ring of G20 adopts a C2′-endo sugar pucker conformation, and its 2′-hydroxyl group engages in hydrogen bonding interactions with Ser145 and Tyr173. These interactions provide a structural basis for the high specificity of Cas6f in recognizing and cleaving pre-crRNA and or pre-RacrIF1, thereby ensuring precise processing of crRNA or Racrs without off-target effects. These interactions also provide a structural explanation for the loss of Cas6f binding and RacrIF1 inhibition caused by the C6G/G20C inversion at the base of the RacrIF1 stem, as reported previouly.[35] By removing the guanosine at position 20, which is directly read out by R99 and stacked against F152, the mutation reverses the major-groove donor/acceptor pattern, dismantles the R99-G20 hydrogen-bonding network and the terminal base-pair stacking platform for F152, and perturbs the active-site geometry that enforces the G20 C2′-endo conformation and positions the scissile phosphate. Consequently, a productive Cas6f-RNA complex cannot form; therefore, cleavage is abrogated.

DISCUSSION

Notably, the physiological relevance of the Cas7f filament structure formed on non-specific RNA remains unclear, and such assemblies are likely biologically irrelevant, as such structures are unlikely to form under normal physiological conditions. *In vivo*, uncontrolled filament formation could be detrimental to the cell, imposing a substantial metabolic burden. Moreover, excessive polymerization of Cas7f on random RNAs would sequester Cas7f proteins and interfere with the assembly of functional CRISPR-Cas complexes. Therefore, cells are likely to employ regulatory mechanisms to restrict Cas7f filamentation, ensuring that polymerization occurs only on cognate crRNA or Racr substrates, and preventing non-productive interactions with non-specific RNAs. We propose several plausible regulatory mechanisms that could operate *in vivo* to restrict non-specific Cas7f filamentation. First, Cas6f-mediated cleavage is essential for the assembly of the crRNA-guided surveillance complex (Csy complex) and RacrIF1-induced aberrant subcomplexes, both of which involve Cas7f. The requirement for mature, Cas6f-cleaved crRNA or RacrIF1 as a prerequisite for the formation of functional complexes provides an efficient natural filtering mechanism *in vivo*. This process likely prevents promiscuous filament formation by Cas7f on non-specific RNAs, which are not recognized or processed by Cas6f. Previous studies have demonstrated that Csy4 (Cas6f) binds crRNA with exceptionally high affinity ($K_D \sim 50$ pM).[49] This high affinity and specificity likely reduce the binding of non-cognate RNA by restricting Cas7f recruitment to properly processed and folded crRNA or RacrIF1, while minimizing interactions with non-specific RNAs.[49] We also performed Cas7f- and/or Cas6f-binding affinity measurements for crRNA, RacrIF1, and non-specific RNA. Both in the presence and absence of Cas7f and/or Cas6f, the binding affinity of Cas7f and/or Cas6f for crRNA and RacrIF1 was significantly higher than for non-specific RNA, regardless of the presence of Cas6f and/or Cas7f (Figures 6A–6C). These data confirm that Cas7f, Cas6f, and Cas7f-Cas6f preferentially binds to mature crRNA and RacrIF1 *in vitro*, with minimal binding to non-specific RNA. Consequently, the binding preference of Cas7f ensures that filament formation is restricted to appropriate crRNA or RacrIF1 targets, thereby preventing filament formation on non-specific cellular RNAs. Second, we employed an

Please cite this article in press as: Gao et al., RNA anti-CRISPRs deplete Cas proteins to inhibit the CRISPR-Cas system, Molecular Cell (2025), https://doi.org/10.1016/j.molcel.2025.12.005

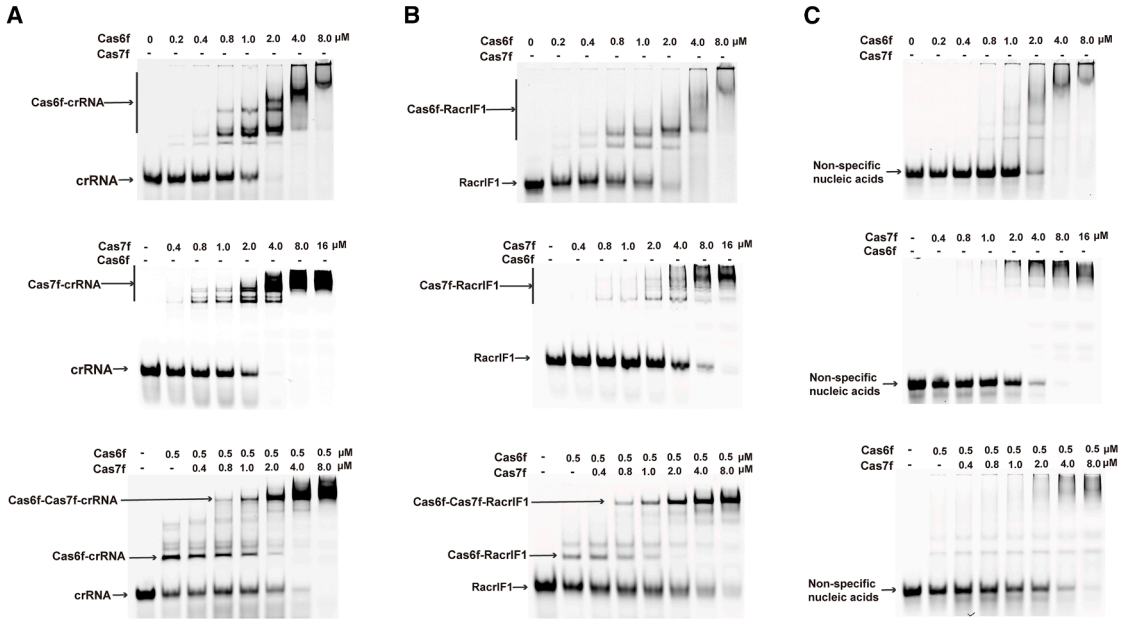

Figure 6. Binding analysis of Cas6f and Cas7f with RNA substrates and the effect of Cas7f on Cas6f-RNA complex formation

(A) EMSAs showing Cas7f and Cas6f binding to crRNA at increasing protein concentrations (0–8 μM Cas6f; 0–16 μM Cas7f). Reactions were also performed by pre-incubating Cas6f with crRNA to assess the effect of Cas7f on Cas6f-crRNA complex formation. Complexes were resolved on native polyacrylamide gels and visualized by fluorescence imaging.

(B) EMSAs showing Cas7f and Cas6f binding to RacIF1 at increasing protein concentrations (0–8 μM Cas6f; 0–16 μM Cas7f). Reactions were also performed by pre-incubating Cas6f with RacIF1 to assess the effect of Cas7f on Cas6f-RacIF1 complex formation.

(C) EMSAs showing Cas7f and Cas6f binding to non-specific RNA at increasing protein concentrations (0–8 μM Cas6f; 0–16 μM Cas7f). Reactions were also performed by pre-incubating Cas6f with non-specific RNA to assess the effect of Cas7f on Cas6f-non-specific-RNA complex formation.

overexpression system for Cas7f, which could lead to excessive accumulation of Cas7f protein, leading to the formation of Cas7f filaments on non-specific RNA. However, in a natural cellular environment, the CRISPR-Cas operon is tightly regulated to maintain a balanced expression of Cas proteins. Both transcriptional and post-transcriptional regulation play crucial roles in controlling CRISPR-Cas systems across many bacterial genomes.[50] This regulatory mechanism prevents overproduction Cas proteins, which could otherwise trigger autoimmunity or cause deleterious effects, thereby imposing a significant metabolic burden on the host.[50,51] For instance, in *P. atrosepticum*, the expression of the type I-F CRISPR-Cas system is tightly controlled by the CRP-cAMP complex in response to glucose availability. The CRP-cAMP complex activates the *cas1* promoter, initiating the expression of the entire *cas* operon.[52] These transcriptional regulatory mechanisms regulate not only the interference stage but also the adaptation stage, ensuring a coordinated and efficient defense response against horizontally acquired genetic elements.[50,52,53] Therefore, it is likely that the latent polymerization ability of Cas7f to form extended filaments on non-cognate RNAs is suppressed by these system-level regulatory mechanisms. Finally, although Cas7f filament structure on non-specific RNA may appear biologically irrelevant, the RacrIF1 processed by Cas6f forms a "functional aberrant Cas subcomplex," which is biologically significant. Given that Cas7f can non-specifically bind nucleic acids and form long filaments, it could theoretically oligomerize infinitely along Racrs, depending on the length of the Racrs. For instance, in a type I-C Racr (RacrIC1), it is likely that Cas7f could bind more units compared with RacrIF1, as RacrIC1 is longer than RacrIF1.[35] The oligomerization of Cas7f on these nucleic acids sequesters Cas6f and Cas7f from their target sites, thereby obstructing the formation of functional CRISPR-Cas effector complexes and ultimately impairing the antiviral immune response. Collectively, our findings demonstrate that the formation of RacrIF1 aberrant Cas subcomplexes requires Cas6f-catalyzed cleavage of pre-RacrIF1 transcripts (Figure 5D), while the Cas7f solenoid complex forms without the involvement of Cas6f.

Phages and MGEs have evolved diverse Acr mechanisms to evade bacterial CRISPR-Cas immunity. Most known type I-F Acr proteins inhibit the fully assembled Csy complex by blocking DNA binding or preventing Cas2/3 recruitment.[25] In contrast, AcrIF25 represents a mechanistically distinct strategy: it binds directly to Cas7f and dismantles the pre-assembled Csy complex by sequentially removing Cas7 subunits in an ATP-independent manner, exposing the crRNA to nuclease attack, and thereby likely causing irreversible inactivation of the complex.[29] By comparison, RacrIF1 adopts a fundamentally different, RNA-based inhibitory strategy that acts upstream of complex assembly. By mimicking the CRISPR repeat, RacrIF1 is recognized and processed by Cas6f, but the absence of a canonical 5′ handle prevents recruitment of Cas5f/Cas8f, and instead promotes an aberrant Cas6f–Cas7f subcomplex that sequesters Cas proteins, thereby blocking cascade formation, interference, and primed adaptation.

Please cite this article in press as: Gao et al., RNA anti-CRISPRs deplete Cas proteins to inhibit the CRISPR-Cas system, Molecular Cell (2025), https://doi.org/10.1016/j.molcel.2025.12.005

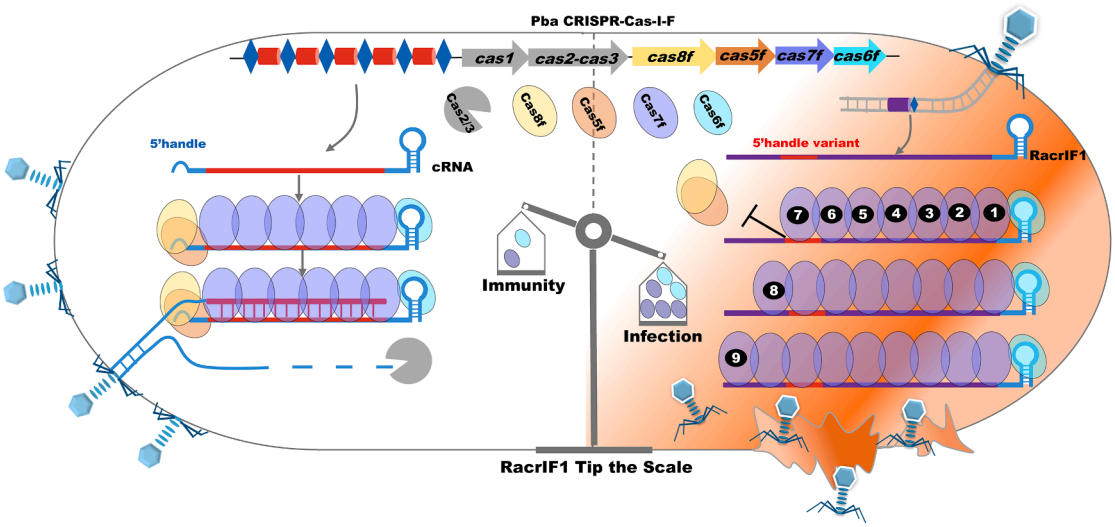

Figure 7. Proposed model for RacrIF1-mediated inhibition of CRISPR-Cas immunity

Mechanistically, RacrIF1 diverts Cas proteins into non-productive assemblies rather than disassembling mature complexes. These two strategies exemplify complementary paradigms of CRISPR-Cas inhibition: protein-based Acrs, such as AcrIF25, irreversibly disassemble existing effectors, whereas RNA-based inhibitors, such as RacrIF1, act as molecular decoys to competitively divert Cas proteins into non-productive assemblies. The frequent co-localization of *racr* and *acr* genes within prophage loci further suggests that RNA- and protein-based Acrs may function synergistically to ensure robust, multilayered suppression of CRISPR-Cas immunity.

Conclusions

Combining our structural and functional studies, we propose a working model for Racrs-mediated inhibition of CRISPR-Cas immunity (Figure 7). In a functional *Pba*-CRISPR-Cas complex, crRNA, bound by Cas6f, serves as a scaffold for Csy complex assembly. The Csy complex recognizes phage DNA and recruits the endonuclease Cas2/3, which degrades the non-target strand to prevent phage infection, thereby maintaining the host's immunity. When RacrIF1 is expressed from the phage genome, it induces the formation of aberrant complexes containing 7–9 Cas7f subunits due to the 5′ handle variant. Cas7f preferentially forms solenoid structures and can theoretically oligomerize infinitely along Racrs, depending on the length of the Racrs. This extensive oligomerization significantly competes with endogenous crRNAs for Cas components, tipping the balance and preventing the formation of functional antiviral CRISPR-Cas effector complexes. As a result, antiviral immunity is blocked, leaving the host susceptible to infection.

Limitations of the study

Our results provide strong evidence for a competition-based mechanism in which Racrs and crRNAs assemble with overlapping pools of Cas proteins. However, we did not directly demonstrate a key element of this model—specifically, that Racrs sequester sufficient Cas7f to deplete the protein from cells and prevent the formation of functional surveillance complexes. This limitation arises because the total cellular pool of Cas7f appears essentially constant, and competition between Racrs and crRNAs likely redistributes Cas7f into distinct assemblies without altering its overall abundance, making direct quantification of Cas7f reduction technically challenging. Nonetheless, direct measurement of Cas7f sequestration under endogenous expression conditions remains an important objective for future studies. Furthermore, our experiments were conducted under protein and RNA overexpression conditions, which may not accurately reflect endogenous expression levels. Future investigations, employing quantitative analyses with endogenously expressed and tagged Cas proteins, will be essential to evaluate Racr-mediated Cas7f sequestration and its impact on surveillance complex assembly under native physiological conditions.

RESOURCE AVAILABILITY

Lead contact

For additional details and inquiries regarding resources and reagents, please contact the lead contact, Sheng Cui (cui.sheng@ipb.pumc.edu.cn), who will handle and provide the necessary assistance.

Materials availability

The plasmids created during this study can be obtained from the lead contact upon completion of a materials transfer agreement.

Data and code availability

- The atomic models of *Pba*-Csy, confor-3, solenoid-1, solenoid-2, and solenoid-3 have been deposited into the Protein Data Bank with accession code 9IRF, 9IRI, 9IRG, 9XCG, and 9XCF, respectively. The corresponding 3D cryo-EM density maps have been deposited into the Electron Microscopy Data Bank under the accession codes EMD-60812 (*Pba*-Csy), EMD-60815 (confor-3), EMD-60813 (solenoid-1), EMD-66731 (solenoid-2), EMD-66729 (solenoid-3), EMD-60817 (confor-1), and EMD-60819 (confor-2), respectively.
- This paper does not report custom code.

- Any additional information required to reanalyze the data reported in this paper is available from the lead contact upon request.

ACKNOWLEDGMENTS

We thank X. Huang, B. Zhu, X. Li, L. Chen, T. Niu, and other staff members at the Center for Biological Imaging (CBI), Core Facilities for protein Science at the Institute of Biophysics, Chinese Academy of Science (IBP, CAS) for the support in cryo-EM data collection. We thank Z.Q. Guo and H.S. Li from Shuimu Biosciences for the cryo-EM data collection. We thank the staff from the Core Facility of National Institute of Pathogen Biology, Chinese Academy of Medical Sciences. This work was supported by Biomedical High Performance Computing Platform, Chinese Academy of Medical Sciences; The Prevention and Control of Emerging and Major Infectious Diseases-National Science and Technology Major Project (2025ZD01901105 and 2025ZD01901100) and the Chinese Academy of Medical Sciences (CAMS) Innovation Fund for Medical Sciences (2024-I2M-TS-22 to X.G. and 2021-I2M-1-037 to S.C. and X.G.); National Natural Science Foundation of China (81971985 and 82272308 to X.G., 81572005 to S.C., and 32471015 to H.Z.); National Natural Science Foundation of China/RGC Joint Research Scheme (no. 82261160398, N_HKU767/22); Chinese Academy of Sciences (nos. E4V4061RA1 and E2VK311RA1); Beijing Natural Science Foundation (7232019); and China Postdoctoral Science Foundation (2025T180775).

AUTHOR CONTRIBUTIONS

X.G. and S.C. designed the study. H.Z. and X.G. solved the EM structures and performed the model building. X.G., S.C., and H.Z. wrote the paper. X.G., K.Z., W.Z., Lin Wang, Linyue Wang, L.H., T.N., X.Y., and B.Q. performed experiments and analyzed the data. All authors reviewed the results and approved the final version of the manuscript.

DECLARATION OF INTERESTS

The authors declare no competing interests.

STAR★METHODS

Detailed methods are provided in the online version of this paper and include the following:

- KEY RESOURCES TABLE
- EXPERIMENTAL MODEL AND STUDY PARTICIPANT DETAILS
  - Bacterial strains and culture conditions
- METHOD DETAILS
  - Plasmid construction
  - Protein expression and purification
  - Urea-PAGE analysis
  - Electrophoretic mobility shift assay (EMSA)
  - *In vitro* DNA cleavage assay
  - Preparation of oligonucleotides
  - Cryo-EM sample preparation
  - Cryo-EM data collection
  - Cryo-EM data analysis
  - Model building
- QUANTIFICATION AND STATISTICAL ANALYSIS

SUPPLEMENTAL INFORMATION

Supplemental information can be found online at https://doi.org/10.1016/j.molcel.2025.12.005.

Received: May 2, 2025
Revised: October 28, 2025
Accepted: December 8, 2025

REFERENCES

1. Hampton, H.G., Watson, B.N.J., and Fineran, P.C. (2020). The arms race between bacteria and their phage foes. Nature *577*, 327–336. https://doi.org/10.1038/s41586-019-1894-8.
2. Mayo-Muñoz, D., Pinilla-Redondo, R., Birkholz, N., and Fineran, P.C. (2023). A host of armor: Prokaryotic immune strategies against mobile genetic elements. Cell Rep. *42*, 112672. https://doi.org/10.1016/j.celrep.2023.112672.
3. Georjon, H., and Bernheim, A. (2023). The highly diverse antiphage defence systems of bacteria. Nat. Rev. Microbiol. *21*, 686–700. https://doi.org/10.1038/s41579-023-00934-x.
4. Tock, M.R., and Dryden, D.T.F. (2005). The biology of restriction and anti-restriction. Curr. Opin. Microbiol. *8*, 466–472. https://doi.org/10.1016/j.mib.2005.06.003.
5. Doron, S., Melamed, S., Ofir, G., Leavitt, A., Lopatina, A., Keren, M., Amitai, G., and Sorek, R. (2018). Systematic discovery of antiphage defense systems in the microbial pangenome. Science *359*, eaar4120. https://doi.org/10.1126/science.aar4120.
6. Gao, L., Altae-Tran, H., Böhning, F., Makarova, K.S., Segel, M., Schmid-Burgk, J.L., Koob, J., Wolf, Y.I., Koonin, E.V., and Zhang, F. (2020). Diverse enzymatic activities mediate antiviral immunity in prokaryotes. Science *369*, 1077–1084. https://doi.org/10.1126/science.aba0372.
7. Gao, Y., Luo, X., Li, P., Li, Z., Ye, F., Liu, S., and Gao, P. (2023). Molecular basis of RADAR anti-phage supramolecular assemblies. Cell *186*, 999–1012.e20. https://doi.org/10.1016/j.cell.2023.01.026.
8. Wang, Y., Guan, Z., Wang, C., Nie, Y., Chen, Y., Qian, Z., Cui, Y., Xu, H., Wang, Q., Zhao, F., et al. (2022). Cryo-EM structures of Escherichia coli Ec86 retron complexes reveal architecture and defence mechanism. Nat. Microbiol. *7*, 1480–1489. https://doi.org/10.1038/s41564-022-01197-7.
9. Payne, L., Jackson, S., and Pinilla-Redondo, R. (2024). Supramolecular assemblies in bacterial immunity: an emerging paradigm. Trends Microbiol. *32*, 828–831. https://doi.org/10.1016/j.tim.2024.06.003.
10. Mohanraju, P., Saha, C., van Baarlen, P., Louwen, R., Staals, R.H.J., and van der Oost, J. (2022). Alternative functions of CRISPR-Cas systems in the evolutionary arms race. Nat. Rev. Microbiol. *20*, 351–364. https://doi.org/10.1038/s41579-021-00663-z.
11. Malone, L.M., Birkholz, N., and Fineran, P.C. (2021). Conquering CRISPR: how phages overcome bacterial adaptive immunity. Curr. Opin. Biotechnol. *68*, 30–36. https://doi.org/10.1016/j.copbio.2020.09.008.
12. Makarova, K.S., Wolf, Y.I., Iranzo, J., Shmakov, S.A., Alkhnbashi, O.S., Brouns, S.J.J., Charpentier, E., Cheng, D., Haft, D.H., Horvath, P., et al. (2020). Evolutionary classification of CRISPR-Cas systems: a burst of class 2 and derived variants. Nat. Rev. Microbiol. *18*, 67–83. https://doi.org/10.1038/s41579-019-0299-x.
13. Barrangou, R., and Marraffini, L.A. (2014). CRISPR-Cas systems: Prokaryotes upgrade to adaptive immunity. Mol. Cell *54*, 234–244. https://doi.org/10.1016/j.molcel.2014.03.011.
14. Wiedenheft, B., Sternberg, S.H., and Doudna, J.A. (2012). RNA-guided genetic silencing systems in bacteria and archaea. Nature *482*, 331–338. https://doi.org/10.1038/nature10886.
15. Hille, F., Richter, H., Wong, S.P., Bratovič, M., Ressel, S., and Charpentier, E. (2018). The Biology of CRISPR-Cas: Backward and Forward. Cell *172*, 1239–1259. https://doi.org/10.1016/j.cell.2017.11.032.
16. Altae-Tran, H., Kannan, S., Suberski, A.J., Mears, K.S., Demircioglu, F.E., Moeller, L., Kocalar, S., Oshiro, R., Makarova, K.S., Macrae, R.K., et al. (2023). Uncovering the functional diversity of rare CRISPR-Cas systems with deep terascale clustering. Science *382*, eadi1910. https://doi.org/10.1126/science.adi1910.
17. Chowdhury, S., Carter, J., Rollins, M.F., Golden, S.M., Jackson, R.N., Hoffmann, C., Nosaka, L., Bondy-Denomy, J., Maxwell, K.L., Davidson, A.R., et al. (2017). Structure Reveals Mechanisms of Viral Suppressors

that Intercept a CRISPR RNA-Guided Surveillance Complex. Cell *169*, 47–57.e11. https://doi.org/10.1016/j.cell.2017.03.012.

18. Guo, T.W., Bartesaghi, A., Yang, H., Falconieri, V., Rao, P., Merk, A., Eng, E.T., Raczkowski, A.M., Fox, T., Earl, L.A., et al. (2017). Cryo-EM Structures Reveal Mechanism and Inhibition of DNA Targeting by a CRISPR-Cas Surveillance Complex. Cell *171*, 414–426.e12. https://doi.org/10.1016/j.cell.2017.09.006.
19. Bondy-Denomy, J., Pawluk, A., Maxwell, K.L., and Davidson, A.R. (2013). Bacteriophage genes that inactivate the CRISPR/Cas bacterial immune system. Nature *493*, 429–432. https://doi.org/10.1038/nature11723.
20. Bondy-Denomy, J., Garcia, B., Strum, S., Du, M., Rollins, M.F., Hidalgo-Reyes, Y., Wiedenheft, B., Maxwell, K.L., and Davidson, A.R. (2015). Multiple mechanisms for CRISPR-Cas inhibition by anti-CRISPR proteins. Nature *526*, 136–139. https://doi.org/10.1038/nature15254.
21. Peng, R., Xu, Y., Zhu, T., Li, N., Qi, J., Chai, Y., Wu, M., Zhang, X., Shi, Y., Wang, P., et al. (2017). Alternate binding modes of anti-CRISPR viral suppressors AcrF1/2 to Csy surveillance complex revealed by cryo-EM structures. Cell Res. *27*, 853–864. https://doi.org/10.1038/cr.2017.79.
22. Wiegand, T., Karambelkar, S., Bondy-Denomy, J., and Wiedenheft, B. (2020). Structures and Strategies of Anti-CRISPR-Mediated Immune Suppression. Annu. Rev. Microbiol. *74*, 21–37. https://doi.org/10.1146/annurev-micro-020518-120107.
23. Davidson, A.R., Lu, W.T., Stanley, S.Y., Wang, J., Mejdani, M., Trost, C.N., Hicks, B.T., Lee, J., and Sontheimer, E.J. (2020). Anti-CRISPRs: Protein Inhibitors of CRISPR-Cas Systems. Annu. Rev. Biochem. *89*, 309–332. https://doi.org/10.1146/annurev-biochem-011420-111224.
24. Pawluk, A., Davidson, A.R., and Maxwell, K.L. (2018). Anti-CRISPR: discovery, mechanism and function. Nat. Rev. Microbiol. *16*, 12–17. https://doi.org/10.1038/nrmicro.2017.120.
25. Yin, P., Zhang, Y., Yang, L., and Feng, Y. (2023). Non-canonical inhibition strategies and structural basis of anti-CRISPR proteins targeting type I CRISPR-Cas systems. J. Mol. Biol. *435*, 167996. https://doi.org/10.1016/j.jmb.2023.167996.
26. Zhang, L., Wang, H., Zeng, J., Cao, X., Gao, Z., Liu, Z., Li, F., Wang, J., Zhang, Y., Yang, M., et al. (2024). Cas1 mediates the interference stage in a phage-encoded CRISPR-Cas system. Nat. Chem. Biol. *20*, 1471–1481. https://doi.org/10.1038/s41589-024-01659-5.
27. Bondy-Denomy, J., Davidson, A.R., Doudna, J.A., Fineran, P.C., Maxwell, K.L., Moineau, S., Peng, X., Sontheimer, E.J., and Wiedenheft, B. (2018). A Unified Resource for Tracking Anti-CRISPR Names. CRISPR J. *1*, 304–305. https://doi.org/10.1089/crispr.2018.0043.
28. Jia, N., and Patel, D.J. (2021). Structure-based functional mechanisms and biotechnology applications of anti-CRISPR proteins. Nat. Rev. Mol. Cell Biol. *22*, 563–579. https://doi.org/10.1038/s41580-021-00371-9.
29. Trost, C.N., Yang, J., Garcia, B., Hidalgo-Reyes, Y., Fung, B.C.M., Wang, J., Lu, W.T., Maxwell, K.L., Wang, Y., and Davidson, A.R. (2024). An anti-CRISPR that pulls apart a CRISPR-Cas complex. Nature *632*, 375–382. https://doi.org/10.1038/s41586-024-07642-3.
30. Rollins, M.F., Chowdhury, S., Carter, J., Golden, S.M., Miettinen, H.M., Santiago-Frangos, A., Faith, D., Lawrence, C.M., Lander, G.C., and Wiedenheft, B. (2019). Structure Reveals a Mechanism of CRISPR-RNA-Guided Nuclease Recruitment and Anti-CRISPR Viral Mimicry. Mol. Cell *74*, 132–142.e5. https://doi.org/10.1016/j.molcel.2019.02.001.
31. Zhang, K., Wang, S., Li, S., Zhu, Y., Pintilie, G.D., Mou, T.C., Schmid, M.F., Huang, Z., and Chiu, W. (2020). Inhibition mechanisms of AcrF9, AcrF8, and AcrF6 against type I-F CRISPR-Cas complex revealed by cryo-EM. Proc. Natl. Acad. Sci. USA *117*, 7176–7182. https://doi.org/10.1073/pnas.1922638117.
32. Gabel, C., Li, Z., Zhang, H., and Chang, L. (2021). Structural basis for inhibition of the type I-F CRISPR-Cas surveillance complex by AcrIF4, AcrIF7 and AcrIF14. Nucleic Acids Res. *49*, 584–594. https://doi.org/10.1093/nar/gkaa1199.
33. Xie, Y., Zhang, L., Gao, Z., Yin, P., Wang, H., Li, H., Chen, Z., Zhang, Y., Yang, M., and Feng, Y. (2022). AcrIF5 specifically targets DNA-bound CRISPR-Cas surveillance complex for inhibition. Nat. Chem. Biol. *18*, 670–677. https://doi.org/10.1038/s41589-022-00995-8.
34. Borges, A.L., Davidson, A.R., and Bondy-Denomy, J. (2017). The Discovery, Mechanisms, and Evolutionary Impact of Anti-CRISPRs. Annu. Rev. Virol. *4*, 37–59. https://doi.org/10.1146/annurev-virology-101416-041616.
35. Camara-Wilpert, S., Mayo-Muñoz, D., Russel, J., Fagerlund, R.D., Madsen, J.S., Fineran, P.C., Sørensen, S.J., and Pinilla-Redondo, R. (2023). Bacteriophages suppress CRISPR-Cas immunity using RNA-based anti-CRISPRs. Nature *623*, 601–607. https://doi.org/10.1038/s41586-023-06612-5.
36. Kraus, C., and Sontheimer, E.J. (2023). Viruses use RNA decoys to thwart CRISPR defences. Nature *623*, 490–491. https://doi.org/10.1038/d41586-023-03133-z.
37. Halpin-Healy, T.S., Klompe, S.E., Sternberg, S.H., and Fernández, I.S. (2020). Structural basis of DNA targeting by a transposon-encoded CRISPR-Cas system. Nature *577*, 271–274. https://doi.org/10.1038/s41586-019-1849-0.
38. Mulepati, S., Héroux, A., and Bailey, S. (2014). Structural biology. Crystal structure of a CRISPR RNA-guided surveillance complex bound to a ssDNA target. Science *345*, 1479–1484. https://doi.org/10.1126/science.1256996.
39. Pausch, P., Müller-Esparza, H., Gleditzsch, D., Altegoer, F., Randau, L., and Bange, G. (2017). Structural Variation of Type I-F CRISPR RNA Guided DNA Surveillance. Mol. Cell *67*, 622–632.e4. https://doi.org/10.1016/j.molcel.2017.06.036.
40. Zhang, M., Peng, R., Peng, Q., Liu, S., Li, Z., Zhang, Y., Song, H., Yang, J., Xing, X., Wang, P., et al. (2023). Mechanistic insights into DNA binding and cleavage by a compact type I-F CRISPR-Cas system in bacteriophage. Proc. Natl. Acad. Sci. USA *120*, e2215098120. https://doi.org/10.1073/pnas.2215098120.
41. Taylor, D.W., Zhu, Y., Staals, R.H.J., Kornfeld, J.E., Shinkai, A., van der Oost, J., Nogales, E., and Doudna, J.A. (2015). Structural biology. Structures of the CRISPR-Cmr complex reveal mode of RNA target positioning. Science *348*, 581–585. https://doi.org/10.1126/science.aaa4535.
42. Hayes, R.P., Xiao, Y., Ding, F., van Erp, P.B.G., Rajashankar, K., Bailey, S., Wiedenheft, B., and Ke, A. (2016). Structural basis for promiscuous PAM recognition in type I-E Cascade from E. coli. Nature *530*, 499–503. https://doi.org/10.1038/nature16995.
43. Hochstrasser, M.L., Taylor, D.W., Kornfeld, J.E., Nogales, E., and Doudna, J.A. (2016). DNA Targeting by a Minimal CRISPR RNA-Guided Cascade. Mol. Cell *63*, 840–851. https://doi.org/10.1016/j.molcel.2016.07.027.
44. Jackson, R.N., Golden, S.M., van Erp, P.B.G., Carter, J., Westra, E.R., Brouns, S.J.J., van der Oost, J., Terwilliger, T.C., Read, R.J., and Wiedenheft, B. (2014). Structural biology. Crystal structure of the CRISPR RNA-guided surveillance complex from Escherichia coli. Science *345*, 1473–1479. https://doi.org/10.1126/science.1256328.
45. Zhao, H., Sheng, G., Wang, J., Wang, M., Bunkoczi, G., Gong, W., Wei, Z., and Wang, Y. (2014). Crystal structure of the RNA-guided immune surveillance Cascade complex in Escherichia coli. Nature *515*, 147–150. https://doi.org/10.1038/nature13733.
46. Rollins, M.F., Chowdhury, S., Carter, J., Golden, S.M., Wilkinson, R.A., Bondy-Denomy, J., Lander, G.C., and Wiedenheft, B. (2017). Cas1 and the Csy complex are opposing regulators of Cas2/3 nuclease activity. Proc. Natl. Acad. Sci. USA *114*, E5113–E5121. https://doi.org/10.1073/pnas.1616395114.
47. Haurwitz, R.E., Sternberg, S.H., and Doudna, J.A. (2012). Csy4 relies on an unusual catalytic dyad to position and cleave CRISPR RNA. EMBO J. *31*, 2824–2832. https://doi.org/10.1038/emboj.2012.107.
48. Haurwitz, R.E., Jinek, M., Wiedenheft, B., Zhou, K., and Doudna, J.A. (2010). Sequence- and structure-specific RNA processing by a CRISPR

endonuclease. Science *329*, 1355–1358. https://doi.org/10.1126/science.1192272.

49. Sternberg, S.H., Haurwitz, R.E., and Doudna, J.A. (2012). Mechanism of substrate selection by a highly specific CRISPR endoribonuclease. RNA *18*, 661–672. https://doi.org/10.1261/rna.030882.111.
50. Shivram, H., Cress, B.F., Knott, G.J., and Doudna, J.A. (2021). Controlling and enhancing CRISPR systems. Nat. Chem. Biol. *17*, 10–19. https://doi.org/10.1038/s41589-020-00700-7.
51. Vale, P.F., Lafforgue, G., Gatchitch, F., Gardan, R., Moineau, S., and Gandon, S. (2015). Costs of CRISPR-Cas-mediated resistance in Streptococcus thermophilus. Proc. Biol. Sci. *282*, 20151270. https://doi.org/10.1098/rspb.2015.1270.
52. Patterson, A.G., Chang, J.T., Taylor, C., and Fineran, P.C. (2015). Regulation of the Type I-F CRISPR-Cas system by CRP-cAMP and GalM controls spacer acquisition and interference. Nucleic Acids Res. *43*, 6038–6048. https://doi.org/10.1093/nar/gkv517.
53. Patterson, A.G., Jackson, S.A., Taylor, C., Evans, G.B., Salmond, G.P.C., Przybilski, R., Staals, R.H.J., and Fineran, P.C. (2016). Quorum Sensing Controls Adaptive Immunity through the Regulation of Multiple CRISPR-Cas Systems. Mol. Cell *64*, 1102–1108. https://doi.org/10.1016/j.molcel.2016.11.012.
54. Punjani, A., Rubinstein, J.L., Fleet, D.J., and Brubaker, M.A. (2017). cryoSPARC: algorithms for rapid unsupervised cryo-EM structure determination. Nat. Methods *14*, 290–296. https://doi.org/10.1038/nmeth.4169.
55. Liebschner, D., Afonine, P.V., Baker, M.L., Bunkóczi, G., Chen, V.B., Croll, T.I., Hintze, B., Hung, L.W., Jain, S., McCoy, A.J., et al. (2019). Macromolecular structure determination using X-rays, neutrons and electrons: recent developments in Phenix. Acta Crystallogr. D Struct. Biol. *75*, 861–877. https://doi.org/10.1107/S2059798319011471.
56. Emsley, P., Lohkamp, B., Scott, W.G., and Cowtan, K. (2010). Features and development of Coot. Acta Crystallogr., D *66*, 486–501. https://doi.org/10.1107/S0907444910007493.
57. Pettersen, E.F., Goddard, T.D., Huang, C.C., Couch, G.S., Greenblatt, D.M., Meng, E.C., and Ferrin, T.E. (2004). UCSF Chimera–a visualization system for exploratory research and analysis. J. Comput. Chem. *25*, 1605–1612. https://doi.org/10.1002/jcc.20084.
58. Pettersen, E.F., Goddard, T.D., Huang, C.C., Meng, E.C., Couch, G.S., Croll, T.I., Morris, J.H., and Ferrin, T.E. (2021). UCSF ChimeraX: Structure visualization for researchers, educators, and developers. Protein Sci. *30*, 70–82. https://doi.org/10.1002/pro.3943.
59. Sun, D., Zhu, K., Wang, L., Mu, Z., Wu, K., Hua, L., Qin, B., Gao, X., Wang, Y., and Cui, S. (2024). Nucleic acid-induced NADase activation of a short Sir2-associated prokaryotic Argonaute system. Cell Rep. *43*, 114391. https://doi.org/10.1016/j.celrep.2024.114391.
60. Gao, X., Shang, K., Zhu, K., Wang, L., Mu, Z., Fu, X., Yu, X., Qin, B., Zhu, H., Ding, W., et al. (2024). Nucleic-acid-triggered NADase activation of a short prokaryotic Argonaute. Nature *625*, 822–831. https://doi.org/10.1038/s41586-023-06665-6.
61. Wu, C., Huang, X., Cheng, J., Zhu, D., and Zhang, X. (2019). High-quality, high-throughput cryo-electron microscopy data collection via beam tilt and astigmatism-free beam-image shift. J. Struct. Biol. *208*, 107396. https://doi.org/10.1016/j.jsb.2019.09.013.
62. Mastronarde, D.N. (2005). Automated electron microscope tomography using robust prediction of specimen movements. J. Struct. Biol. *152*, 36–51. https://doi.org/10.1016/j.jsb.2005.07.007.
63. Zheng, S.Q., Palovcak, E., Armache, J.P., Verba, K.A., Cheng, Y., and Agard, D.A. (2017). MotionCor2: anisotropic correction of beam-induced motion for improved cryo-electron microscopy. Nat. Methods *14*, 331–332. https://doi.org/10.1038/nmeth.4193.
64. Rohou, A., and Grigorieff, N. (2015). CTFFIND4: Fast and accurate defocus estimation from electron micrographs. J. Struct. Biol. *192*, 216–221. https://doi.org/10.1016/j.jsb.2015.08.008.
65. Bepler, T., Morin, A., Rapp, M., Brasch, J., Shapiro, L., Noble, A.J., and Berger, B. (2019). Positive-unlabeled convolutional neural networks for particle picking in cryo-electron micrographs. Nat. Methods *16*, 1153–1160. https://doi.org/10.1038/s41592-019-0575-8.
66. Scheres, S.H.W. (2012). RELION: implementation of a Bayesian approach to cryo-EM structure determination. J. Struct. Biol. *180*, 519–530. https://doi.org/10.1016/j.jsb.2012.09.006.
67. Grant, T., Rohou, A., and Grigorieff, N. (2018). cisTEM, user-friendly software for single-particle image processing. eLife *7*, e35383. https://doi.org/10.7554/eLife.35383.
68. Sanchez-Garcia, R., Gomez-Blanco, J., Cuervo, A., Carazo, J.M., Sorzano, C.O.S., and Vargas, J. (2021). DeepEMhancer: a deep learning solution for cryo-EM volume post-processing. Commun. Biol. *4*, 874. https://doi.org/10.1038/s42003-021-02399-1.
69. Abramson, J., Adler, J., Dunger, J., Evans, R., Green, T., Pritzel, A., Ronneberger, O., Willmore, L., Ballard, A.J., Bambrick, J., et al. (2024). Accurate structure prediction of biomolecular interactions with AlphaFold 3. Nature *630*, 493–500. https://doi.org/10.1038/s41586-024-07487-w.
70. Adams, P.D., Afonine, P.V., Bunkóczi, G., Chen, V.B., Davis, I.W., Echols, N., Headd, J.J., Hung, L.W., Kapral, G.J., Grosse-Kunstleve, R.W., et al. (2010). PHENIX: a comprehensive Python-based system for macromolecular structure solution. Acta Crystallogr., D *66*, 213–221. https://doi.org/10.1107/S0907444909052925.

Please cite this article in press as: Gao et al., RNA anti-CRISPRs deplete Cas proteins to inhibit the CRISPR-Cas system, Molecular Cell (2025), https://doi.org/10.1016/j.molcel.2025.12.005

STAR★METHODS

KEY RESOURCES TABLE

REAGENT or RESOURCE	SOURCE	IDENTIFIER
Bacterial and virus strains		
E. coli strain BL21 (DE3)	NEB	Cat# C2527
E. coli DH5α	Vazyme	Cat# C505-02
Chemicals, peptides, and recombinant proteins		
Kanamycin Sulfate	INALCO	Cat#1758-9316
IPTG	INALCO	Cat#1758-1400
Ampicillin Sodium Salt	INALCO	Cat#1758-9314
Prestained Protein Marker	Vazyme	Cat#MP102-01
Phenylmethyl sulfonyl fluoride	MACKLIN	Cat#P815753
TCEP	MACKLIN	Cat#T819166
Chloramphenicol	Solarbio	Cat#C8050
EDTA	Solarbio	Cat#E1170
$MgCl_2 \cdot 6H_2O$	Merck	Cat#930989
DpnI	Thermo Scientific	FD1703
Critical commercial assays		
SYBR™ Gold	Invitrogen	Cat#S11494
2 × Phanta Flash Master Mix	Vazyme	Cat#P510
Urea-PAGE Gel	Wshtbio	Cat#E301U15F
In-Fusion® HD Cloning Kit	TaKaRa	Cat#639649
Deposited data		
Structure of *Pba-Csy*	This paper	PDB: 9IRF; EMD-60812
Structure of Confor-3	This paper	PDB: 9IRI; EMD-60815
Solenoid-1	This paper	PDB: 9IRG; EMD-60813
Solenoid-2	This paper	PDB: 9XCG; EMD-66731
Solenoid-3	This paper	PDB: 9XCF; EMD-66729
Confor-1	This paper	EMD-60817
Confor-2	This paper	EMD-60819
Oligonucleotides		
See Table S4	Genscript	N/A
Recombinant DNA		
pQE60-*cas8f-cas5f-cas7f*	This paper	N/A
pRSFDuet-*His-cas6f-crRNA*	This paper	N/A
pRSFDuet-*His-cas6f-RacrIF1*	This paper	N/A
pQE60-*His-cas8f-cas5f-cas7f*	This paper	N/A
pQE60-*cas8f-cas5f-His-cas7f*	This paper	N/A
pQE60-*cas7f*	This paper	N/A
pET28a-*His-sumo-cas7f*	This paper	N/A
pRSFDuet-*RacrIF1*	This paper	N/A
pRSFDuet-*crRNA*	This paper	N/A
pRSFDuet-*cas6f-crRNA*	This paper	N/A
pRSFDuet-*cas6f-RacrIF1*	This paper	N/A
pRSFDuet-*His-cas6f*	This paper	N/A
pET28a-*His-cas8f-cas5f*	This paper	N/A
pETDuet-*His-cas1-cas2/3*	This paper	N/A

(*Continued on next page*)

Please cite this article in press as: Gao et al., RNA anti-CRISPRs deplete Cas proteins to inhibit the CRISPR-Cas system, Molecular Cell (2025), https://doi.org/10.1016/j.molcel.2025.12.005

Continued

REAGENT or RESOURCE	SOURCE	IDENTIFIER
pACYCDuet-*crRNA*	This paper	N/A
pRSFDuet-*cas6f*	This paper	N/A
Software and algorithms		
cryoSPARC	Punjani and Fleet[54]	https://cryosparc.com/
Phenix	Liebschner et al.[55]	https://phenix-online.org/
COOT	Emsley and Cowtan[56]	https://www2.mrc-lmb.cam.ac.uk/personal/pemsley/coot/
UCSF Chimera	Pettersen et al.[57]	https://www.cgl.ucsf.edu/chimera/
UCSF ChimeraX	Pettersen et al.[58]	https://www.rbvi.ucsf.edu/chimerax/
PyMOL	Schrödinger	https://pymol.org/2/
Origin 8.0	OriginLab	https://www.originlab.com/
Other		
Ni-NTA Agarose	QIAGEN	Cat#30230
Superdex 200 Increase 10/300 GL	Cytiva	Cat#28-9909-44
HiTrap Heparin HP	Cytiva	Cat#17040701
HiTrap Q HP	Cytiva	Cat#17115301
Amicon concentrators (30K)	Millipore	Cat#UFC903024

EXPERIMENTAL MODEL AND STUDY PARTICIPANT DETAILS

Bacterial strains and culture conditions

Escherichia coli DH5α cells were used for cloning construction and plasmid extraction. *Escherichia coli* BL21(DE3) cells were used for expressing recombinant proteins. All the strains were grown in LB medium at 37 °C. The final concentrations of antibiotics were used as follows: Kanamycin, 50 μg/mL; Ampicillin, 100 μg/mL; Chloramphenicol, 30 μg/mL.

METHOD DETAILS

Plasmid construction

The operon encoding Cas8f, Cas5f, and Cas7f was synthesized by GenScript and subsequently cloned into the pQE60 vector between the MunI and HindIII restriction sites to produce plasmid pQE60-*cas8f-cas5f-cas7f*, incorporating a ribosome binding site sequence at the N-terminus of the genes. Individually synthesized RacrIF1 and crRNA were subsequently cloned into the pRSFDuet-1 vector. The insertion was carried out at the NdeI and XmaJI restriction sites located within the MCS2 region, resulting in the construction of pRSFDuet-*crRNA* and pRSFDuet-*RacrIF1*, respectively. The *cas6f* gene, synthesized by GenScript, was PCR-amplified and cloned into the pRSFDuet-1 vector at the BamHI and HindIII restriction sites or Nco1 and HindIII within MCS1, which already contained RacrIF1 or crRNA in MCS2, to produce the His-tagged or non-tagged Cas6f-RacrIF1/crRNA (pRSFDuet-*His-cas6f-RacrIF1*/crRNA or pRSFDuet-*cas6f-RacrIF1*/*crRNA*). For the expression of the Cas7f-RacrIF1 complex, the *cas7f* gene was PCR-amplified and cloned into the pRSFDuet-1 vector at the BamHI and HindIII restriction sites within MCS1, while *RacrIF1* was already cloned into MCS2 to produce pRSFDuet-*His-cas7f-RacrIF1*. To express the Cas6f-Cas7f-RacrIF1 complex, the plasmid for expressing Cas7f was constructed by deleting the *cas8f-cas5f* genes from the pQE60-*cas8f-cas5f-cas7f* vector, resulting in the pQE60-*cas7f* plasmid. This plasmid was used to co-express the pRSFDuet-*His-cas6f-RacrIF1*. For the expression of the Cas8f-Cas5f complex, the *cas8f-cas5f* gene was cloned into the pET28a vector at the NdeI and XhoI restriction sites to produce pET28a-*His-cas8f-cas5f*. For the His-pull down assay, His tags were added to the N-termini of Cas8f or Cas7f on the plasmid pQE60-*cas8f-cas5f-cas7f* using a site-directed mutagenesis strategy to produce pQE60-*His-cas8f-cas5f-cas7f* or pQE60-*cas8f-cas5f- His-cas7f*. This modified plasmid was then co-expressed with non-tagged pRSFDuet-*cas6f-RacrIF1*/*crRNA*. For the co-expression of RacrIF1 and the Csy complex, the plasmid pACYCDuet-*crRNA* was constructed. To express Cas7f, the corresponding gene was cloned into the pET28a-His-sumo vector. For the expression of Cas1-Cas2/3 proteins, the *cas1* and *cas2/3* genes synthesized by GenScript were inserted into the pETDuet-1 vector between the BamHI/HindIII and NdeI/XhoI restriction sites, respectively, resulting in the construction of the pETDuet-*His-cas1-cas2/3* plasmid. The complete list of synthesized genes and primers can be found in Tables S2 and S3.

Protein expression and purification

To express and purify the *Pba*-Csy complex and aberrant Cas subcomplexes, the pQE60-*cas8f-cas5f- His-cas7f* and either pRSFDuet-*cas6f-RacrIF1*/*crRNA* plasmids were co-transformed into *E. coli* BL21(DE3) cells. These cells were selected using

Please cite this article in press as: Gao et al., RNA anti-CRISPRs deplete Cas proteins to inhibit the CRISPR-Cas system, Molecular Cell (2025), https://doi.org/10.1016/j.molcel.2025.12.005

kanamycin and ampicillin resistance. The *E. coli* BL21(DE3) cells were cultivated in LB medium at 37°C with shaking at 180 rpm until the optical density at 600 nm (OD600) reached 0.8. Protein expression was induced by adding isopropyl-β-D-thiogalactopyranoside (IPTG) to a final concentration of 0.25 mM, followed by incubation at 18°C with shaking at 160 rpm for 16 hours. The cells were harvested by centrifugation at 3,470×g for 10 minutes at 4°C, and resuspended in lysis buffer containing 50 mM HEPES (pH 7.4), 300 mM KCl, 10 mM imidazole, 5% glycerol, and 1 mM phenylmethylsulfonyl fluoride (PMSF). The cells were lysed by sonication and centrifuged at 40,000 x g for 60 minutes at 4°C. The supernatant containing the soluble proteins was collected and incubated with Ni-NTA resin pre-equilibrated with the lysis buffer. The resin was washed with lysis buffer to remove non-specifically bound proteins, and the target proteins were eluted with elution buffer containing 20 mM HEPES (pH 7.4), 100 mM KCl, 5% glycerol, and 250 mM imidazole. The proteins were concentrated by ultrafiltration and subjected to further purification using a Superdex 200 Increase 10/300 GL column (Cytiva) in gel filtration buffer (20 mM HEPES, pH 7.4, 100 mM KCl). The peak fractions containing the target protein were analyzed using SDS-PAGE and Urea-PAGE. The expression and purification of the Cas6f-Cas7f-RacrIF1 and Cas7f-RacrIF1 complexes were performed using the same protocols as those established for the *Pba*-Csy complex. Similarly, the Cas1-Cas2/3 complex was purified following the procedure described for the *Pba*-Csy complex, with the exception that protein expression was induced with 0.1 mM IPTG. For the co-expression of RacrIF1 and the Csy complex, the plasmids pQE60-*cas8f-cas5f-His-cas7f*, pRSFDuet-*cas6f-RacrIF1*, and pACYCDuet-*crRNA* were co-transformed into *E. coli* BL21(DE3) competent cells. Protein expression and purification were then carried out under the same conditions as described above.

For the expression and purification of the Cas8f-Cas5f complex, the procedure was similar with the following modifications: the lysis buffer contained 50 mM Tris-HCl (pH 8.0), 150 mM NaCl, and 10 mM imidazole. For the purification of Cas7f, the lysis buffer was composed of 50 mM Tris–HCl (pH 8.0), 2 M NaCl, and 10 mM imidazole. Similarly, for the purification of Cas6f, the lysis buffer contained 50 mM Tris–HCl (pH 8.0), 500 mM NaCl, and 10 mM imidazole, while the elution buffer contained 20 mM Tris-HCl (pH 8.0), 50 mM NaCl, and 300 mM imidazole. Eluted samples were further purified using a HiTrap Q HP column (GE Healthcare) or Heparin HP column equilibrated with a buffer containing 20 mM Tris-HCl (pH 8.0) and 25 mM NaCl. The target protein was eluted with a NaCl gradient from 10 mM to 1 M. The fractions containing the target protein were finally purified by size-exclusion chromatography using a Superdex 200 Increase 10/300 GL column (Cytiva) pre-equilibrated with a storage buffer containing 20 mM Tris-HCl (pH 8.0) and 100 mM NaCl.

Urea-PAGE analysis

RNA samples expressed under different constructs were isolated and purified using phenol-chloroform extraction followed by ethanol precipitation, and then dissolved in DEPC-treated water. The purified RNA was then mixed with loading buffer (Thermo Fisher Scientific) and separated on a 15% denaturing urea-PAGE gel using 1×TBE buffer for 70 minutes as previously describely.[59,60] Following electrophoresis, the gels were stained with SYBR GOLD (Thermo Fisher Scientific) and visualized with a ChemiDoc Imaging System (Bio-Rad).

Electrophoretic mobility shift assay (EMSA)

The EMSA was performed as previously described.[60] RNA containing sulfo-cyanine 3 (Cy3) labeled at the 3′ terminus was synthesized by GenScript. A concentration of 0.25 μM of the labeled RNA was incubated with 0-8 μM of the Cas8f-Cas5f complex in a buffer consisting of 20 mM HEPES (pH 7.4), 100 mM KCl, 5% glycerol, 2 mM MgCl2, and 0.5 mM TCEP for 30 minutes at 25°C. The resulting mixtures were then loaded onto a 6% native PAGE gel and run in 0.5×TBE buffer (Solarbio) at 100 V for 50 minutes at 4°C. Visualization of the Cy3-labeled RNA in the gel was performed using a ChemiDoc MP Imaging System (Bio-Rad).

In vitro DNA cleavage assay

Target and non-target bubble DNAs were annealed at a molar ratio of 1.5:1 to generate double-stranded bubble DNA (dsDNA). The *in vitro* DNA cleavage reaction was performed following previously described protocols with slight modifications.[33] Briefly, 0.04 μM dsDNA was incubated with 0.32 μM Csy complex or Csy aberrant complex at 37 °C for 30 min in a reaction buffer containing 20 mM HEPES (pH 7.4), 100 mM KCl, 5% glycerol, and 1 mM TCEP. Subsequently, Cas1-Cas2/3 was added to a final concentration of 0.5 μM, together with 5 mM $MgCl_2$, 75 μM $NiSO_4$, 5 mM $CaCl_2$, and 2 mM ATP. The mixture was further incubated at 37 °C for 0, 10, 30, or 60 min, after which the reaction was quenched with 1% SDS and 50 mM EDTA. The products were separated by 15% urea-PAGE at 150 V for 50 min, and visualized by fluorescence imaging.

To examine the competitive effect of RacrIF1, 0.32 μM Csy complex was pre-incubated with 0.4, 0.8, 1.6, or 3.2 μM RacrIF1 at 37 °C for 30 min in a reaction buffer containing 20 mM HEPES (pH 7.4), 100 mM KCl, 5% glycerol, and 1 mM TCEP. Then, 0.04 μM dsDNA was added and incubated for another 30 min. Finally, 0.5 μM Cas1-Cas2/3, 5 mM $MgCl_2$, 75 μM $NiSO_4$, 5 mM $CaCl_2$, and 2 mM ATP were added, and the reaction was continued at 37 °C for 60 min before termination with 1% SDS and 50 mM EDTA. Reaction products were analyzed as described above. For the *in vivo* competition assay, mixtures containing both functional Csy complex(0.32μM) and aberrant Csy complexes (0.32-2.56 μM) were used to replace the Csy complex in the reaction. All other experimental conditions and procedures were identical to those described for the *in vitro* assays.

Please cite this article in press as: Gao et al., RNA anti-CRISPRs deplete Cas proteins to inhibit the CRISPR-Cas system, Molecular Cell (2025), https://doi.org/10.1016/j.molcel.2025.12.005

Preparation of oligonucleotides

The crRNA, RacrIF1, 5′ handle, 5′ handle variant, 5′ handle-S, 5′ handle variant-S, and other 5′ handle variants, as well as the DNA substrates used for nuclease activity assays, were chemically synthesized and purchased from GenScript. The corresponding sequences are listed in Table S4.

Cryo-EM sample preparation

Cryo-EM grids were prepared using a FEI Vitrobot Mark IV. For all sample, a volume of 2.5 μL of concentrated protein at a concentration of 3.5 mg/mL was applied to 200 mesh Quantifoil 2/2 gold grids, which had been pre-treated using an Easiglow discharge cleaning system. The grids were blotted with filter paper for 2.5 seconds at a blotting force setting of 1 in an environment with 100% humidity. Subsequently, the grids were rapidly plunged into liquid ethane pre-cooled by liquid nitrogen. The grids were then stored in liquid nitrogen until they were used for cryo-EM data collection.

Cryo-EM data collection

The datasets were collected at the Center for Biological Imaging, Core Facilities for Protein Science, Institute of Biophysics, Chinese Academy of Sciences and at Shuimu Biosciences. At the Institute of Biophysics, Chinese Academy of Sciences, movies were recorded on a FEI Titan Krios microscope equipped with a K3 detector, operating at an acceleration voltage of 300 kV. Data acquisition was performed at a nominal magnification of 29,000x, resulting in a pixel size of 0.83 Å. The defocus range was set between -1.5 and -2.5 μm. The movies were collected by SerialEM[61,62] or EPU with a total electron dose of 66 $e^{-}/Å^{2}$. At the Shuimu BioSciences, the cryo-EM datasets were obtained on a Titan Krios microscope equipped with a Gatan Falcon4 direct detection camera, with a pixel size of 0.82 Å and a defocus range of -1.5 μm to -2.5 μm. Each micrograph was dose-fractionated into 32 frames, with a total accumulated dose between 50 and 60 $e^{-}/Å^{2}$.

Cryo-EM data analysis

For the dataset involving the purified type I-F *Pba*-Cascade with RacrIF1, a total of 13,196 movies were recorded. Following motion correction[63] and CTF estimation[64] in cryoSPARC-3.3.2,[54] approximately 885,000 particles were picked using Blob picker. One round of 2D classification was performed to isolate the good particles, selecting 3,499 particles with tubular features for further analysis of the Solenoid-1 structure. Topaz[65] training was then conducted using these selected particles, resulting in the extraction of 13,198 particles by Topaz,[65] followed by ab-initio reconstruction. To determine the initial helical parameters, we first estimated the helical pitch and rise using the *Volume Tracer* tool in UCSF Chimera. A *Symmetry Search* was subsequently performed in cryoSPARC with a helical pitch range of 60-90 Å and a subunit turn count of 7-9, yielding refined parameters of 80.72 Å for the helical pitch and -50.03° for the helical twist. The subsequent helical refinement produced high-resolution density maps for the Solenoid-1 structure, revealing well-resolved subunit features.

To determine the structures of Confor-1, Confor-2, and Confor-3, corresponding 2D classes were selected, and ab-initio reconstruction was performed to generate the 3D models. A template picker was then used, yielding 2.774 million particles. Four rounds of heterogeneous refinement were performed to screen the good particles, resulting in 162,000 particles that were kept for one round of non-uniform refinement. The particles were converted to Relion format using pyem,[66] and CisTEM[67] was utilized for 30 rounds of focused 3D classification, producing maps for Confor-1, Confor-2, and Confor-3. Notably, approximately 89,000 particles corresponding to Confor-3 were imported back to cryoSPARC-3.3.2[54] to enhance resolution through non-uniform refinement. The final resolutions reported for Confor-1, Confor-2, and Confor-3 were 3.7 Å, 3.2 Å, and 2.8 Å, respectively.

For the Solenoid-2 dataset, 5,409 movies were collected. Following motion correction[63] and CTF estimation[64] in cryoSPARC-3.3.2,[54] After Blob picking, around 485,000 particles were extracted and binned by 2. 2D classification was employed to discard non-tube-like particles, retaining approximately 128,000 particles for ab-initio reconstruction. The subsequent processing of Solenoid-2 was identical to that of Solenoid-1, leading to enhanced map quality and consistent reconstruction across all solenoids.

For the Solenoid-3 dataset, a total of 1,243 movies were collected. After motion correction[63] and CTF estimation[64] in cryoSPARC v3.3.2,[54] 193,634 particles were automatically picked using the Blob picker and binned by 2. One round of 2D classification was performed to remove poor-quality and non-tubular particles, retaining 123,551 good particles for further processing. The selected particles were subjected to ab-initio reconstruction, followed by heterogeneous refinement to identify the best-resolved 3D class. Subsequent Topaz particle picking and helical refinement were performed with optimized parameters (helical twist, -50.03°; helical rise, 11.64 Å), yielding a high-quality density map at 4.58 Å resolution after deepEMhancer post-processing. For the *Pba*-Csy complex dataset, 7,064 movies were recorded. motion correction[63] and CTF estimation[64] were carried out in cryoSPARC-3.3.2.[54] Approximately 1.4 million particles were picked using Blob picker in cryoSPARC-3.3.2[54] and one round of 2D classification was performed to identify the good particles. Five 3D initial models were generated via ab-initio reconstruction, with three favorable classes selected for another round of heterogeneous refinement using particles directly from Blob picker. Two classes containing 347,000 and 518,000 particles were chosen for one round of heterogeneous refinement. Subsequently, one class with good Cas5f and Cas8f density, harboring 424,000 particles, was selected for focused classification in CisTEM.[67] After 30 rounds of focused 3D classification in CisTEM,[67] the best class with optimal Cas5f and Cas8f density was chosen. Approximately 71,806 particles were kept and imported back to cryoSPARC-3.3.2[54] for non-uniform refinement, achieving a final resolution of 2.8 Å for the *Pba*-Csy complex. All of the maps were finally optimized and sharpened using DeepEMhancer.[68]

Model building

Before building the models, we generated homology structures of Cas5f, Cas6f, Cas7f, and Cas8f using AlphaFold3.[69] Model building was initiated with the *Pba*-Csy complex. Utilizing prior knowledge, we created an initial model in UCSF Chimera[57] by rigid body fitting of one Cas5f, one Cas6f, six Cas7f, one Cas8f, and crRNA to the map. Coot[56] was then used for manual refinement of the structure against the map, and the crRNA was manually built in in Coot,[56] resulting in the construction of 60 nucleotides. Phenix real-space refinement in PHENIX[70] was employed to further refine the structure.

For constructing the Cas7 solenoid structure, we fit Cas7f subunits to the solenoid map in UCSF Chimera.[57] Random nucleic acids were manually built in Coot,[56] and Phenix real-space refinement in PHENIX[70]was used to refine the structure against the map. All helical solenoid maps (Solenoid-1, Solenoid-2, and Solenoid-3) were reoriented by z-flipping before model building.

To build the Confor-3 structure, we started with the *Pba*-Csy complex and deleted the chains for Cas8f and Cas5f in Coot.[56] We then placed two additional Cas7f subunits into the map by rigid body fitting in UCSF Chimera.[57] The nucleic acids were manually built in Coot,[56] resulting in a total of 69 nucleotides modeled. After several rounds of manual refinement in Coot,[56] Phenix real-space refinement in PHENIX[70] was used to further refine the structure. Representative EM Densities of Various Complexes are shown in Figure S10.

QUANTIFICATION AND STATISTICAL ANALYSIS

For details of the cryo-EM image-processing workflow, see the STAR Methods and Figures S2 and S5. Atomic models were built in COOT, refined with Phenix, and validated statistically in Table S1. For fluorescence-labeled nucleic acid electrophoresis, imaging was performed with a ChemiDoc MP system, and each experiment was repeated at least twice.